



School of Chemistry

Studying the Oxidation of Diamond Using an O₂ Plasma Reactor

James Bird

This thesis is submitted in partial fulfilment of the requirements for the Honours Degree of MSci at the University of Bristol

Submitted 02/07/17

Supervisor: Professor Paul May
Second Assessor: Dr Neil Fox
Physical and Theoretical

Abstract

H-terminated diamond is found to exhibit a negative electron affinity (NEA), and as such could find applications in field emission devices such as thermionic energy convertors (TECs). However, labile C-H surface bonds thermally decompose and provoke concomitant NEA loss. O-termination of a diamond surface gives a positive electron affinity (PEA), but subsequent metallation re-establishes NEA. This project used the simple technique of contact angle (CA) measurements to quantify the oxidation of as-grown polycrystalline diamond surfaces. Diamond samples were oxidized using a custom-built O₂ plasma reactor, converted from a sputter coater. This reactor was optimized for oxidation using a statistical approach, a Taguchi orthogonal array.

Uniform polycrystalline diamond samples were grown using hot filament chemical vapour deposition (HFCVD) and characterized prior to oxidation using laser Raman spectroscopy and scanning electron microscopy (SEM). Wettability analysis using the sessile drop method with various liquid phases permitted calculation of diamond surface free energy (SFE). The Owens-Wendt method allowed separation of SFE in to its polar and dispersed components. CA measurements using water as a liquid phase allowed quantification of oxidized surface species. X-ray photoelectron spectroscopy (XPS) was used to support CA measurements and identify oxygen-containing surface moieties.

Taguchi optimization suggested low voltage (1.16 kV) and low pressure (0.1 Torr) plasma operating conditions gave the smallest CAs. XPS analysis identified a component within the C1s binding energy region at 285.5 – 285.8 eV, which appears essential for small CAs. Although a sample modified in accordance with the results of the Taguchi analysis failed to harbour the largest percentage atomic oxygen concentration across analysed samples.

Acknowledgements

Naturally I would like to thank everyone in the Diamond Group for their persistent help, but most of all I thank James Smith for his never-ending will to assist and for his optimism. I extend my gratitude to Michael and Fabian for all their help with everything XPS-related and to Dr Robert Harniman for eternally entertaining the idea of TUNA analysis despite our inability to convene. I must also thank my supervisors, Professor Paul May and Dr Neil Fox for their support and guidance throughout the year.

Finally, I thank all my friends and family who have helped me through this awful year. There were points where I thought I'd never see this project to the end, but look where we are now.

All of this has been for you Dad. I wish only that you were here to see it.

1. Table of Contents

2. Introduction.....	6
1.1 Diamond Synthesis.....	7
2.1.1. CVD Reactors	9
2.1.2. Growing Conditions.....	11
i Epitaxy and Nucleation.....	11
ii Gas Composition.....	11
2.2. Diamond Structure.....	13
2.2.1. (111).....	14
2.2.2. (100).....	16
2.3. Surface Characterisation Techniques.....	17
2.4. Wettability	18
2.5. Oxygen termination.....	21
2.5.1. Electrochemical oxidation	22
2.5.2. Thermal oxidation	22
2.5.3. Wet chemical oxidation	25
2.5.4. Oxygen-plasma termination.....	25
2.6. Electronic Conductivity	27
3. Instrumentation and Techniques.....	32
3.1. CVD diamond growth	32
3.1.1. Instrumentation	32
3.1.2. Standard Operation.....	36
3.2. Scanning Electron Microscopy (SEM)	38
3.3. Wettability	40
3.4. O₂ Plasma Reactor	43
3.4.1. Instrumentation	43
3.4.2. Standard Operation.....	46
3.5. Laser Raman Spectroscopy	49
3.6. X-ray Photoelectron Spectroscopy (XPS)	51
4. Experimental Method	53
4.1. Preliminary Investigation.....	53
4.2. Surface free energy (SFE) calculation.....	54

4.3. Taguchi Optimization.....	54
4.4. XPS	58
5. Results.....	60
5.1. SEM	60
5.2. Laser Raman Spectroscopy	61
5.3. Preliminary investigation.....	62
5.4. SFE calculation.....	65
5.5. Taguchi Optimization.....	69
5.6. XPS.....	73
6. Discussion.....	79
6.1. SEM	79
6.2. Laser Raman Spectroscopy	79
6.3. Preliminary investigation.....	80
6.4. SFE calculations.....	84
6.5. Taguchi Optimization.....	85
6.6. XPS.....	89
7. Conclusions and Further Work	95

2. Introduction

Diamond is omnipresent in the modern world: synonymous with beauty and wealth and known as a material of superlative physical characteristics in materials science¹. Since the rejuvenation of diamond popularity in the mid 19th century, with the discovery of huge diamond deposits in Africa that assisted in the continuing rise of the British Empire², and further aided by war-fuelled technological advancements in the 1930's, its uses have evolved considerably. This carbon allotrope was named after its indestructible nature and heralded for its elegance. Today, with the growth of technology and knowledge, its allure has been redirected towards the development of superior materials that harness its unique properties³. Unparalleled qualities of single-crystal diamond include thermal conductivity, Young's modulus and Vickers hardness; hence the drive to conceive uses for this one-of-a-kind crystal.

Yet in the search for facile diamond synthesis methods, polycrystalline diamond has taken the foreground in recent research efforts, harnessing different, though highly applicable properties to single-crystal diamond. Polycrystalline diamond synthesised via chemical vapour deposition (CVD) techniques currently finds itself in niche specialist applications like in electrodes and simple sensors⁴. Although with efficient CVD diamond synthesis techniques now being commonplace, researchers are looking to modify these polycrystalline surfaces to revolutionize engineering. Accompanying an accumulation of understanding of the diamond surface structure is an ability to fine-tune diamond surface properties. An intriguing property of H-terminated diamond is its negative electron affinity (NEA). Exploiting this property would open this material to more desirable applications like field-emission technologies, but the C-H surface bonds are unstable at high temperatures. Oxidation followed by metallisation could provide the necessary stabilization, but only if we can understand and achieve controlled oxygen-termination of diamond surfaces.

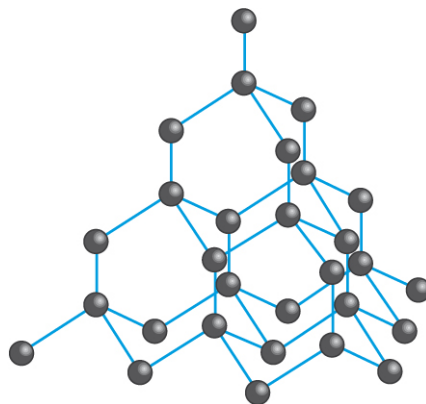


Figure 1: The sp^3 covalently hybridised lattice of the archetypal group (IV) diamond structure.

1.1 Diamond Synthesis

Carbon is like all other elements in that it too has a phase diagram⁵, albeit somewhat unusual. Bundy and many others worked on this diagram, with a complete picture being provided in 1989, which aids in illustrating the issues that confronted scientists in facile diamond synthesis. According to the phase diagram, the stable form of carbon is graphite at atmospheric temperature and pressure, and diamond formation occurs only at very high temperatures and pressures. Diamonds in nature are found far below sea level, which inspired the first, successful diamond synthesis method: HPHT (High Pressure High Temperature)⁶. High pressure (>120 kbar) and high temperature (3000°C) permits the direct conversion of the stable allotrope graphite to diamond.

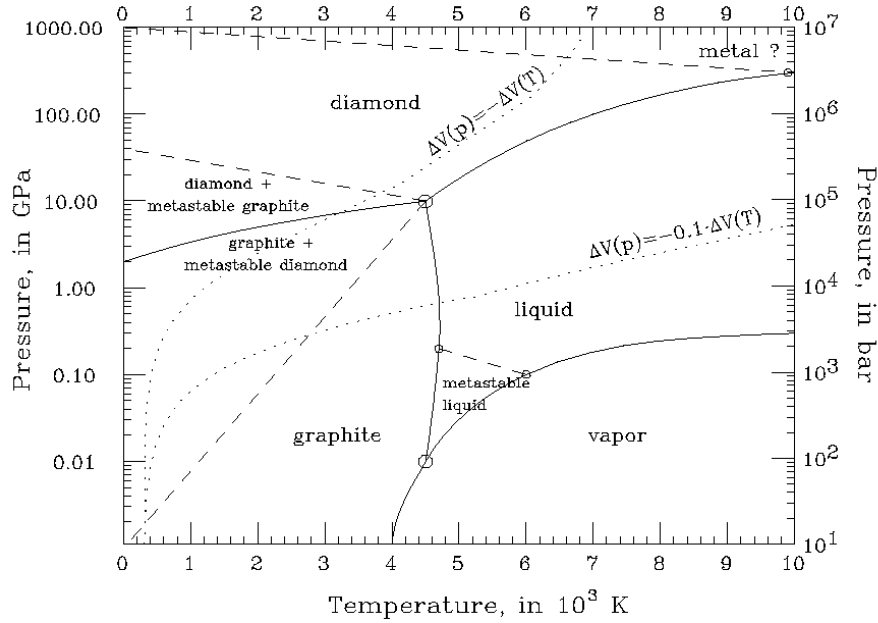


Figure 2: Carbon Phase Diagram⁷.

These extreme conditions were of course not economically viable, which led to the development of the much more popular HPHT method of diamond growth as developed by General Electric (GE) in the 80s. GE commercialized a solvent-catalyst reaction mechanism that introduced a transition metal to the reaction medium, as such providing an alternative, catalytically lowered transition state pathway, reducing the energy of activation E_a for the allotropic conversion reaction. The diminished reaction conditions were appreciably more economically viable and succeeded in the fabrication of monocrystals.

Analysis of the thermodynamics of graphite and diamond conversion shows that graphite has an enthalpy a mere 2 kJ/mol lower than that of diamond. Direct conversion, however, requires that the large enthalpy of activation must be overcome, demonstrating the kinetic restraints of diamond formation. Polycrystalline diamond synthesis was born with the development of CVD

techniques. Instead of the direct conversion of graphite to diamond, this method builds diamond from individual hydrocarbon sub-units, usually being methane. CVD affords the synthesis of mainly polycrystalline diamond and bypasses the use of extreme temperatures and pressures. CVD techniques therefore produce metastable diamond, as the enthalpic barrier to graphite formation doesn't permit direct interconversion at room temperature and pressure. Metastable product formation requires fine-tuning of conditions, which after years of research have been successfully optimized and more importantly, understood.

2.1.1. CVD Reactors

The basic principle of a CVD reactor is that gaseous carbonaceous reactants are activated above the substrate surface to allow step-wise growth from short hydrocarbons. Activation of the gaseous mixture has been most successfully achieved in the form of 2 different reactor types:

- Hot Filament CVD (HFCVD)
- Plasma-Assisted CVD (PACVD)

HFCVD places a filament of W, Rh or Ir 0.5-2 cm above the substrate surface allowing gas activation through heating to 2000-2400°C. Atomic H production is of the order of 2-10%⁸ which is essential in the removal of unwanted graphitic layers, as atomic H etches graphitic sp² carbon significantly faster than sp³ carbon found in diamond. Heating the substrate further supports improved diamond quality although the substrate is somewhat heated by the filament also.

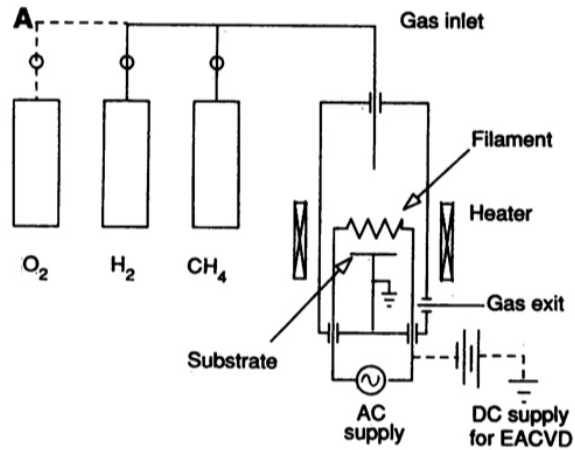


Figure 3: HFCVD reactor schematic diagram⁹.

One of the more common PACVD techniques is microwave CVD (MWCVD), which employs a microwave source to form glow-discharge non-isothermal plasma in the reactor. The high-frequency electric field of 2.45 GHz created by the microwaves couples with the electrons of the gaseous atoms, causing them to rapidly accelerate and consequently ionise. Upon collision of the electrons with the newly created ions, dissociation occurs giving high-energy reactive intermediates. This active gaseous phase or plasma provides precursor molecules capable of interacting with the substrate surface.

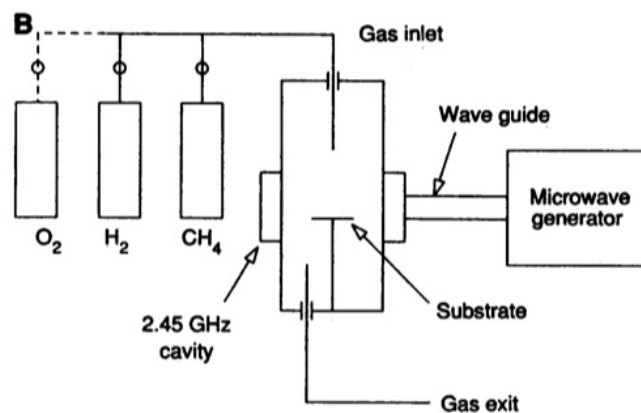


Figure 4: MWCVD reactor schematic diagram⁹.

2.1.2. Growing Conditions

i Epitaxy and Nucleation

Homoepitaxial growth, although possible, occurs at a very slow rate and would render diamond growth expensive due to the high cost of natural diamond. Therefore heterogeneous diamond synthesis has been greatly advanced since Jiang *et al.* remarked its success in 1993¹⁰. As with any heteroepitaxial deposition, thermal expansion and lattice constants for the substrate and depositing material must be similar to encourage *in-situ* geometry replication and to prevent fissure formation on substrate contraction/expansion. Silicon substrates have been heavily researched and have been found to give reliable diamond films. Despite the similarities in lattice structure and thermal expansion constants, the nucleation event requires initiation, which can be achieved via numerous methods including scratching, substrate seeding and carburization of the substrate⁶. Diamond growth would be simply too slow without pre-treatment of the non-diamond substrate. One of the simpler techniques here is seeding, by which submicron diamond powder etches the substrate surface. Seeding provides nucleation sites for diamond growth and in the process the surface becomes scratched, as such further enhancing diamond growth rate. Scratching/seeding is known to reduce the nucleation delay in CVD reactors notably through providing homoepitaxial growth sites, surface oxide removal and providing sharp edges/kinks with reduced interfacial energy allowing diamond formation through a lower energy transition pathway¹¹.

ii Gas Composition

CVD techniques require the activation of a gaseous reaction mixture of carefully controlled composition. Much higher concentrations of H₂ over CH₄ are understood to allow graphite etching via various proposed mechanisms. Atomic H is assumed to abstract a hydrogen atom on the sp³ diamond surface, forming dihydrogen and allowing the reactive species (normally radical •CH₃) to homolytically attack.

0.1-2 vol% CH₄ in H₂ permits high-quality diamond growth at a reasonable rate through successfully relieving the build-up of side-by-side allotropic graphite synthesis.

This idea of etching is conceptually simple when we consider the sp³ lattice in diamond. Upon abstraction of atomic hydrogen on the diamond surface, a 'dangling bond' forms, leaving a radical surface species. To alleviate this high energy build up the surface radical has few reactive routes available to it, namely:

- 1) React with atomic H to give hydrogen terminated diamond
- 2) React with the reactive species •CH₃ to extend the diamond crystal
- 3) Reconstruct the surface via the formation of low energy penta-, hexa- or heptacyclic carbon rings

Surface reconstruction favours the formation of the lowest energy extended sp² cyclohexene network i.e. graphite synthesis. Therefore in maintaining high hydrogen concentrations, the most likely outcome is hydrogen termination, although any graphite formed in the process is etched, again thanks to atomic H. As a result of these mechanisms, diamond growth by CVD is slow yet efficient and capable of growing diamond films up to 1 mm thick² and on large substrates. Furthermore, this hydrogen termination and consequent avoidance of graphite synthesis retains the desirable NEA property.

2.2. Diamond Structure

Diamond is a pure carbon allotrope consisting of sp^3 carbon atoms bound to 4 others in a face-centred cube (fcc) arrangement with half its tetrahedral vacancies filled, as shown:

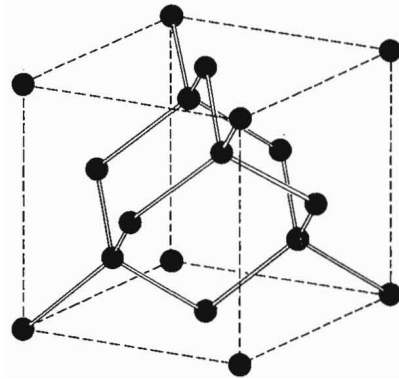


Figure 5: Primitive cell of diamond crystal structure.

When the diamond is cleaved or growth ceases, surfaces are exposed, of which a limited number exists. The most common low-index surface planes of diamond, described by Miller indices (100), (110) and (111), are depicted below. The (111) plane can also be referred to as 'cubic' due to its cubic close packing (ccp) distribution of atomic layers whilst the (100) plane is 'hexagonal' due to its hexagonal close packing (hcp) nature. In order to truly understand oxidation of the diamond surface we must primarily characterise the surface structure with various characterisation techniques, supported by *a priori* surface structure calculations. The dominant diamond growth surfaces in CVD diamond are the (100) and (111) planes¹², so we will focus mainly on those.

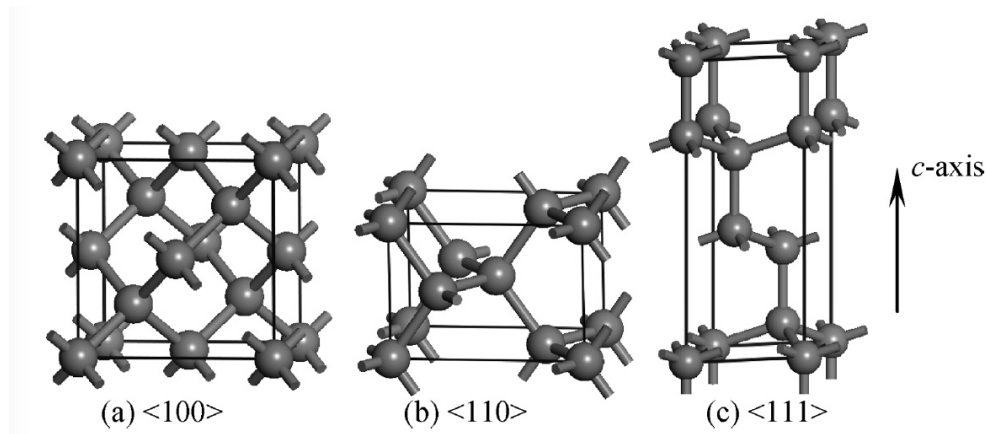


Figure 6: Low-index crystal planes of diamond¹³.

2.2.1. (111)

Initial calculations were undertaken by Adamson¹⁴ based on the single dangling bond per carbon scission theory of the (111) plane, which yielded a high value for surface energy of 5650 mJ/m². Such a large value of surface energy suggests there exists a drive for the diamond surface to rearrange to form other lower energy structures, or alternatively, to react. Especially when we compare the figure to that of the analogous (111) crystal plane of silicon, which yields a value of 1240 mJ/m², whilst metallic zinc yields a surface energy¹⁵ of 105 mJ/m². Alternatively, Halcioglu¹⁶ used a molecular dynamics simulation with a time-step of 0.5×10^{-17} s at 100 K to approximate surface energies for the 3 diamond surfaces depicted above. Potential energy surfaces were assimilated using the Brenner and Tersoff forcefields, with both methods supplying markedly lower surface energies than that described by Adamson. The (111) plane was found to have a surface energy (γ_e) of 4040 and 2662 mJ/m² using the Tersoff and Brenner forcefields, respectively, for an unrelaxed surface (i.e. rigid, non-dynamic model like that used by Adamson). Once the crystal structures had been allowed to relax the surface energy decreased even further with 2772 and 1390 mJ/m², again using Tersoff and Brenner respectively. Relaxation of the rigid crystal lattice manifested itself in all crystal planes through

negligible lateral motion, yet contraction was observed between the first two planes of the surface and expansion between the next two. No significant surface reconstruction to graphitic sp^2 structures was reported, although attention must be drawn to the fact that these molecular dynamics simulations were carried out at low temperature (100 K), hence limited thermal motion was present in the system. It's worth mentioning that the Tersoff and Brenner forcefields, although analytically equivalent, differently define the interactions between bodies, hence explaining the variation in resulting surface energy calculations.

Kern *et al.*¹⁷ argued that the surface energies of an exposed (111) plane cleavage, possessing either 1 or 3 dangling bonds (1db or 3db) dependent on the direction of growth, would differ. Through the use of *ab-initio* local energy density function calculations, several findings were brought to light. Firstly, they found that clean cleavage in a vacuum would invoke π -bonded Pandey chain formation for a 1db per carbon surface (Fig. 7), yet at equilibrium a hydrogen monolayer would give a relaxed C(111)-(1 \times 1):H surface. The clean 3db-C(111) surface adopts the Seiwatz chain geometry (Fig. 7) whilst a hydrogen monolayer retains the topology and merely reduces chain buckling. 2 hydrogen atoms per carbon gives parallel rows of C₂H₄ units and finally 3 hydrogen atoms per surface carbon gives rise to a the 3db-C(111)-(1 \times 1) structure which is equivalent to that of the 1db C(111)-(1 \times 1):H surface with a hydrogen monolayer but with methyl (-CH₃) groups in place of hydrogen (Fig. 7). Calculations show that in fact the more saturated 3db structures are more energetically favoured than for the 1db H-terminated surface, when at higher hydrogen chemical potentials, just as in CVD diamond growth. Scholze *et al.*¹⁸ also supported these findings, yet didn't extend to modelling H-terminated surfaces through total energy-minimizing calculations also using density-function theory in the local-density approximation. Other surface structures are very similar in energy and therefore reconstruction and coexistence in polycrystalline CVD grown diamond is possible.

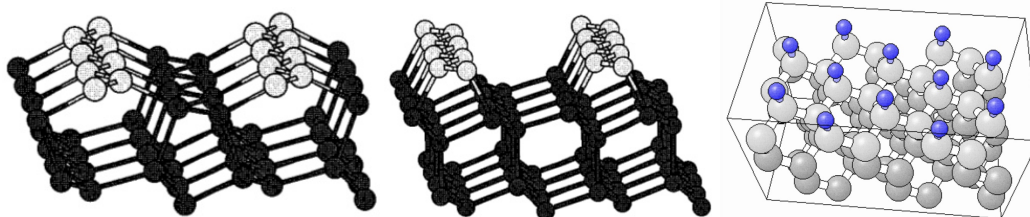


Figure 7: Perspective views of energy-minimised (111) diamond surfaces (left - π -bonded Pandey chains; centre - Seiwatz chains) and the C(111)-(1×1):H surface structure (right)¹⁸.

2.2.2. (100)

The (100) surface has 2 dangling bonds per carbon atom and has also been studied through *a priori* surface structure calculations¹⁹. Yu *et al.* characterized the hydrogen-terminated (100) plane using *ab initio* density-function theory calculations with ultrasoft pseudopotentials. The most stable surface structure is the monohydrogenated C(100)-(2×1):H surface (Fig. 8) which forms surface dimers but at higher hydrogen chemical potentials the dihydrogenated surface becomes the most stable phase. As before with the (111) surface, other surface structures have been known to exist and are thus can coexist, as proven by surface analysis techniques.

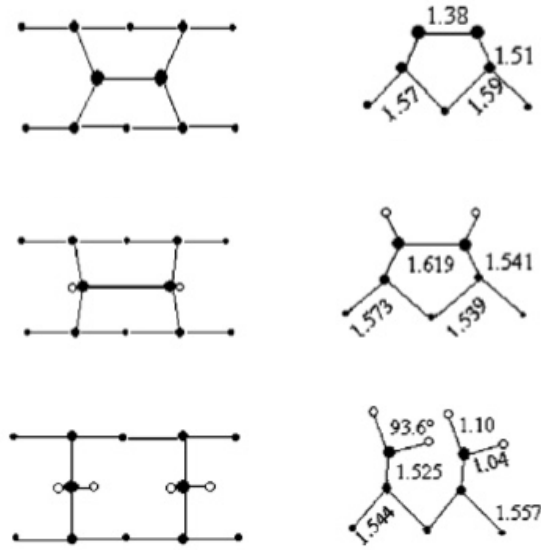


Figure 8: Top (left) and side (right) views of the (100) clean (2×1) surface (top), (2×1):1H surface (centre) and (1×1):2H surface (centre). Black circles represent carbon atoms whilst white circles represent hydrogen ¹⁹.

2.3. Surface Characterisation Techniques

Characterisation of diamond films can and has been performed experimentally using a wide variety of techniques. Some of the more commonly used instruments include Raman and Fourier-transform infrared spectroscopy (FTIR). The latter technique shows a diagnostic peak at 2800-2970 cm^{-1} corresponding to the $\nu_{\text{C-H}}$ stretching frequency of an sp^3 hybridized carbon²⁰, allowing easy detection of successful diamond H-termination.

Most analytical surface chemistry techniques require samples to be under high vacuum, which can attain pressures as low as 10^{-9} Torr, as in ultra-high vacuum (UHV). Examples of analytical methods that require high vacuum (10^{-6} Torr) or UHV conditions are Auger electron spectroscopy (AES), scanning electron microscopy (SEM), tunnelling atomic force microscopy (TUNA), X-ray photoelectron

spectroscopy (XPS) and NanoESCA. The latter is a more advanced XPS analytical technique that provides nanoscale resolution. All of these high vacuum/UHV techniques prove to be excellent for surface characterisation, although attaining such high vacuum requires specialist, expensive equipment. Unfortunately, this fact renders these tools not economically viable for persistent use.

Other options available for surface analysis are Rutherford backscattering (RBS) and low-energy electron diffraction (LEED).

2.4. Wettability

A simple, cheap method for ensuring the success of surface oxidation uses wettability. The sessile drop method is one of the more simple techniques, which involves placing a droplet of a liquid medium on a surface and then measuring the angle between the surface and the droplet as pictured.

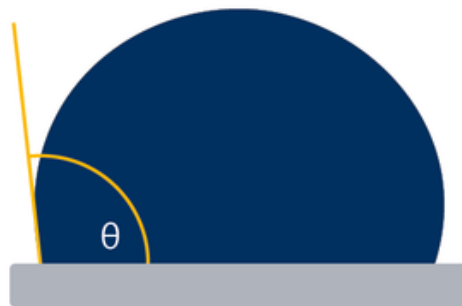


Figure 9: Sessile drop method for static contact angle measurement demonstrating the position of the contact angle when a liquid droplet (blue semicircle) is placed on a solid surface (grey rectangle)²¹.

Acknowledgement of the variation in contact angle (CA) and thus surface hydrophobicity provides information on the physical and chemical properties that manifest themselves through the surface. The surface hydrophobicity²² changes between hydrogen-terminated and oxygen-terminated diamond. As such, studies have shown hydrogen-terminated surfaces to be significantly more hydrophobic than their oxidized counterparts. Ostrovskaya *et al.*²² performed CA measurements and found the CAs with water as a liquid phase measured $\theta=93^\circ$ and $\theta=32^\circ$ for hydrogen-terminated and oxygen-terminated CVD diamond surfaces, respectively. This phenomenon is accounted for because water, a polar liquid phase, interacts more strongly with the strongly heteropolar oxidized surface than the hydrogenated surface whom also possesses a heteropolar dipole, but a much weaker one due to the similarity in electronegativity of carbon and hydrogen.

Despite this method giving an impression of simplicity, the results are in fact highly reproducible ($\pm 1-2^\circ$)^{22,23}, and with a variety of wetting media (including glycerin, tin and water) it is possible to calculate surface energies, γ_e . Using three different liquid phases on the same surface with known polar and dispersion components allows calculation of the solid-phase surface energy using Fowke's law²⁴ as shown below:

$$W_a = \sqrt{\gamma_{lv}^p \gamma_{sv}^p} + \sqrt{\gamma_{lv}^d \gamma_{sv}^d} = \gamma_{lv}(1 + \cos \theta) \quad (1)$$

Here W_a is the work of adhesion, γ_{ij}^p and γ_{ij}^d represent the surface energies of polar and dispersed components, respectively. The subscript letters indicate between which phases the surface energies correspond: liquid (l), vapor (v) and solid (s) phases, respectively. Therefore γ_{lv} corresponds to the sum of the surface energies for the polar and dispersed components between the liquid and vapor phase, whilst θ describes the surface-wetting angle.

Ostrovskaya *et al.*²² found the surface free energies to be 47 and 65.8 mJ/m² for hydrogenated and oxidized diamond surfaces, respectively, therefore significantly less than calculated theoretically. The paper reports a strong correlation between wettability and the sp² or sp³ nature of the surface due to treatment of surfaces with hydrogen plasma, rendering it more graphitic and yielding a lower surface energy.

As briefly demonstrated, wetting measurements are subject to many variables. Again, Ostrovskaya *et al.*²² remarked on the extreme sensitivity of CA measurements to impurities on the surface, even in small quantities, whilst Hansen²⁵ highlighted the effect of hysteresis, especially when using water due to its hydrogen-bonding nature. Water possesses an inherent hysteretic nature that limits the reproducibility of results as it is assumed to stay physisorbed to surface microcracks. Water vapour present in air is capable of displaying this phenomenon through condensation on the surface, consequently lowering successive CA measurements. This effect is enhanced by the heterogeneity of the surface, especially once oxidized. Oxidation of the diamond surface is known to give a wide variety of higher oxidation level species including carbonyl (C=O), lactone (-(CO)O-), carboxylic acid (CO₂H), cyclic ether (COC)^[20] and hydroxyl (COH) groups²⁵. The varying proportions of these groups provokes discontinuities in the amount of hydrogen bonding with the liquid phase (especially when water) therefore influencing CAs.

To minimise the variability in CA measurements some groups have used extensive cleansing and polishing regimes. An example of such a regime is shown in the work of Hansen *et al.*^[25] where they first gave natural diamond a preliminary polish followed by ultrasound washing with Contrad detergent, final polishing with sub-micron grain alumina, further ultrasound washing in 3 changes of Milli-Q water before finally drying with indirect heat at 150°C under nitrogen.

Yet another factor that has been found to affect CA measurements is the surface roughness²⁶. Wenzel stressed the importance of distinguishing the difference between the geometric, completely smooth surface and the actual surface of a material through the formulation of the aptly named Wenzel equation:

$$\cos \theta_W = r \cos \theta_Y \quad (2)$$

Here, θ_Y is the measured CA for the value originally found in Young's equation (hence the γ) for measuring interfacial energies, and r is the roughness factor which relates the two types of surface area described above, always providing a value greater than 1. As is clear, micron-sized crystals, as produced through CVD techniques, would have a much-increased actual surface area compared to that of the geometric area. It is not unusual, therefore, for groups to polish their samples to a certain roughness²². It is possible to somewhat neglect this phenomenon through the assumption that all CVD diamond films grown under the same conditions and duration should have approximately the same roughness.

2.5. Oxygen termination

Oxygen termination of diamond has been achieved through many alternative pathways that can be subdivided into 4 main categories: electrochemical oxidation, thermal oxidation, wet chemical oxidation and oxygen-plasma termination. Other techniques exist including photochemical procedures and ozone exposure, however these are less commonly employed²⁷.

2.5.1. Electrochemical oxidation

Sugata *et al.*²⁸ and Kaibara *et al.*²⁹ successfully carried out electrochemical oxidation on the nanometre scale using AFM voltage-bias anodic oxidation: an analogous mechanism to electrochemical anodic oxidation. Albeit an incredible achievement allowing almost atomic scale surface architecture modifications, this novel technique is costly, time-consuming and not applicable to large-scale surface oxidation.

2.5.2. Thermal oxidation

Ostrovskaya²² thermally oxidised diamond films in air at 500°C for 0.5 hours. Sappok³⁰ and Ando²⁰ both undertook similar thermal oxidations over a range of temperatures in order to explore the mechanisms by which hydrogen-terminated diamond surfaces, like those produced through CVD growth, are oxidized. Ando used diamond powder in a tubular flow reactor with 20% oxygen in argon for a range of times with treatment temperatures ranging from 300-1000°C, whereas Sappok³⁰ explored the temperature range of 25-900°C. Hansen *et al.*²⁵ employed a temperature-controlled tube furnace also, although it was restricted to 450°C as they found heating diamond in an oxygen atmosphere above 500°C provoked etching of diamond to graphitic sp² carbon.

Sappok *et al.* agreed with these latter findings as they noted that treatment with O₂ at 800-900°C and 0.1-10 Torr formed graphitic black carbon, although they also offered practical insight into the mechanism of oxidation. At these higher temperatures the diamond surface is being constantly oxidized, affording desorption of CO₂ and CO. As the surface originally possessed a C:O ratio of ~1-2, the

loss of oxygen-containing gaseous compounds with a ratio C:O of ≤ 1 leaves singly unbound carbon atoms. Under high O₂ pressure further oxidation occurs through O₂ chemisorption. Yet at lower O₂ pressures these carbon atoms can rearrange to form surface dimers that are graphitic in nature. This model seems to accurately interpret the etching of diamond films through low-pressure oxidation, although Ando *et al.* allegedly did not observe this same event, potentially suggesting 20% oxygen is sufficient to prevent etching.

Ando and Sappok found correlating data, independently of one another, displaying the oxidation/hydrogen abstraction of the diamond surface is complete at 410-420°C, characterised by the use of all dangling carbon bonds in surface bonds. Calculations give the estimated number of dangling bonds on low-index crystal planes and thus using temperature-programmed reaction (TPR) allowed the percentage coverage of oxygen to be determined through the sample's weight gain. Furthermore, the two groups calculated that maximum surface oxidation occurs at ~480°C. A combination of thermoanalytical and spectroscopic techniques allowed Ando *et al.* to propose step-wise oxidation mechanisms as a function of reaction temperature. Analysis techniques included Fourier-transform infrared spectroscopy (FTIR), thermogravimetry (TG), temperature-programmed desorption (TPD), differential temperature analysis (DTA) and TPR. Note the hydrogen-terminated diamond was entirely stable below 300°C. They proposed a 3-stage process as depicted below:

- A. Dehydrogenation and oxygenation (300-380°C) – The hydrogen-terminated diamond is oxidized by O₂, eliminating water and forming cyclic-ethers (a.k.a. bridging oxygens) and carbonyl functional groups (Fig. 10).

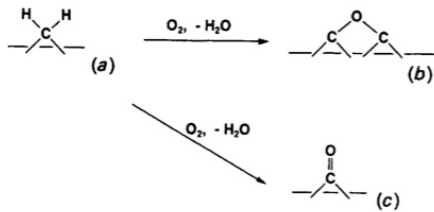


Figure 10: Dehydrogenation and oxygenation process of H-terminated diamond surface at $T=300-380^{\circ}\text{C}$.

B. Further oxygenation ($380-480^{\circ}\text{C}$) – cyclic ethers are further oxidized to lactones which can yet further oxidize to anhydride (Fig. 11).

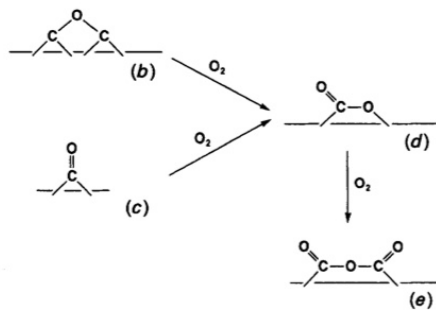


Figure 11: Further oxygenation processes in temperature range $T=380-480^{\circ}\text{C}$.

C. Desorption ($>500^{\circ}\text{C}$) – anhydrides are liable to decarboxylation and therefore further oxidation of the departing carbon above 500°C (Fig. 12). Can be considered as burning off/combustion.

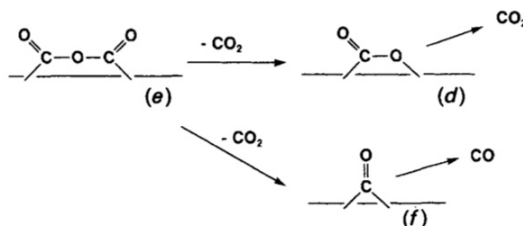


Figure 12: Desorption process at $T>500^{\circ}\text{C}$.

As mentioned, there appears to be some ambiguity about the conversion of surface sp^3 carbon to sp^2 graphite-like structures. Ando refutes the etching process through their FTIR observations below 500°C: although an unidentified peak exists in the spectrum, which some groups have accounted for as an sp^2 C-H stretching frequency ($\nu_{C-H} = 1444 \text{ cm}^{-1}$), there is no corresponding sp^2 C-H stretching frequency as would usually be found in the 3000-3200 cm^{-1} region.

2.5.3. Wet chemical oxidation

Many commonplace acidic oxidation mixtures have been found to function on diamond surfaces. Sappok *et al.* submerged natural diamond powder in sodium hypochlorite (NaClO) and nitric acid solutions whilst Gribanova boiled CVD diamond for 20 minutes in a chromic acid mixture and in a mixture of hydrochloric and nitric acids. However Gribanova noted the risk of using such hard oxidation techniques on a CVD diamond surface when some parts of the film were destroyed during the boiling process.

2.5.4. Oxygen-plasma termination

Szunerits' review paper on diamond surface functionalization stated the best way of oxygen-terminating a hydrogen-terminated diamond surface is with an oxygen-plasma³¹. However, such a bold claim appears to be wildly unfounded seeing as just a handful of papers report oxygen-plasma termination, and amongst the few there are, a detailed account of the successes and failings are not attained. Work carried out by Notsu *et al.*^{32,33} shows the success of oxygen-plasma termination, as confirmed by marked changes in the hydrophilicity of CVD diamond films, analysed through CA measurements, even after just 60 s of plasma exposure. One paper³¹

explores oxygen-plasma termination of as-grown H-terminated CVD diamond films with constant power (100 W) and pressure (20 Pa) but with varying exposure times. XPS surface characterisation confirmed that after a 60 s deposition a sharp O 1s peak and a clearly discernible O KLL Auger peak appeared.

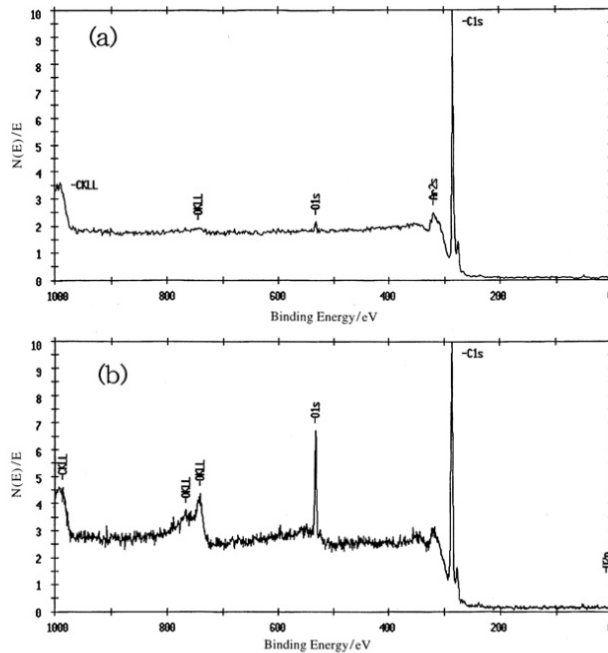


Figure 13: XPS spectra for an a) hydrogen-terminated and b) 60 s oxygen-plasma treated diamond sample³².

The group observed that after long periods of oxygen-plasma termination (>10 min) the surface became significantly rougher, however for oxidation processes during 1-60s there was no noticeable variation on the micrometre scale. Non-variable surface roughness is important when concerned with yielding reproducible wetting angles, as explored earlier.

Of the many functional groups detected on oxidized diamond surfaces, Notsu *et al.*³³ suggest that different low-index crystal planes in diamond harbour different

moieties. On a boron-doped diamond (BDD) surface the (100) oxidized plane possesses carbonyl (C=O) and cyclic-ether (C-O-C) groups whilst the (111) plane with its single dangling bond possesses hydroxyl (C-OH) groups. Hydroxyl presence is confirmed through chemical modification with a silane coupling agent that cannot react with carboxyl, carbonyl or ether groups and further backed up by Hansen *et al.*²⁵ through reaction with ferric ions and later wetting analysis.

2.6. Electronic Conductivity

The electronic properties of diamond have been extensively studied alongside the development of CVD techniques, which facilitated diamond property manipulation, therefore launching the field of diamond electrochemistry. Boron-doped diamond found use in electrodes (anodes in particular) due to its ease of synthesis and range of desirable properties. A BDD anode would be especially useful in water treatment thanks to its corrosion stability, high efficiency and background current amongst other characteristics³⁴.

The need to dope diamond stems from the fact that a perfect diamond would be considered an insulator due to the absence of free electrons, much unlike a metal, thus the presence of defects and/or dopants renders it semi-conducting as in Type IIb boron-containing natural diamond³⁵. Diamond doping with boron is well documented and has been successfully introduced in to the diamond lattice as a gas through CVD techniques as early as 1973³⁶. Band theory describes an insulator and a semi-conductor in much the same manner; the difference between the two is a question of magnitude of band gap between valence and conduction bands³⁷. The diagram below depicts this variation:

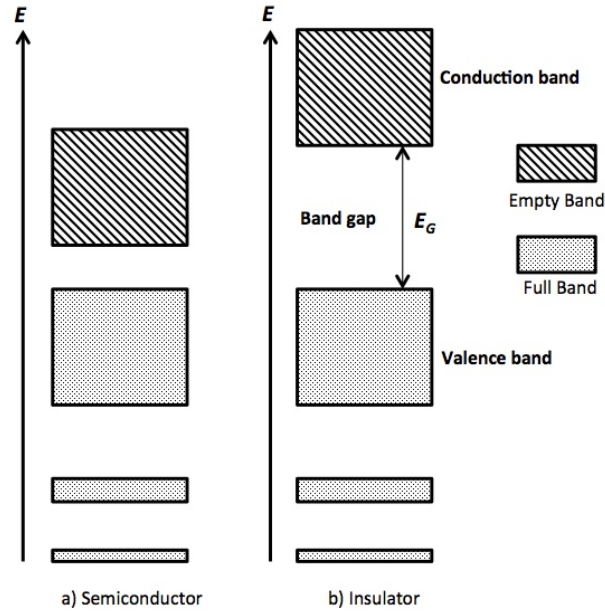


Figure 14: Schematic diagram representing allowed and forbidden energy bands for a) a semiconductor and b) an insulator. Reproduced from source^[35].

As can be seen, in both an insulator and a semiconductor the valence band is filled whilst the conduction band is empty. However a semiconductor possesses a band gap of $E_G = 0.1 - 2.5 \text{ eV}$ whilst an insulator has a band gap of $E_G \geq 3 \text{ eV}$. The smaller band gap of semiconductors enables electrons to transfer from the valence band maximum (VBM) to the conduction band minimum (CBM) in the presence of adequate thermal excitation. This promotion of electrons follows the Fermi-Dirac distribution, which describes the probability of band population and resembles a Boltzmann distribution when $T > 0$ and $E \gg E_F$, as is true for a semiconductor at room temperature. Occupation of the conduction band on the application of an electric field leaves holes in the valence band, thus the mobilisation of electrons and said holes renders the material (semi-) conducting³⁸.

In order to explain how the presence of boron converts diamond to a semiconductor we need to explore a slightly more complicated picture than that provided above. Boron, possessing one less valence electron per atom than carbon, is the only element capable of slotting directly in to the carbon lattice due to their similarity in ionic radius. Hence electron-deficient trivalent boron can accept an electron from carbon leaving 'holes' in the valence band which carry a positive charge. Described above is the formation of a classical p-type semiconductor where boron provides an accessible 'acceptor level' just 0.37 eV above the valence band³⁹, which enables electron transfer from the VBM provided sufficient thermal energy is present⁴⁰. Thus insulating diamond with its wide band gap of 5.5 eV becomes a semiconductor with the addition of this low-lying acceptor level, opening diamond up to numerous electronic applications.

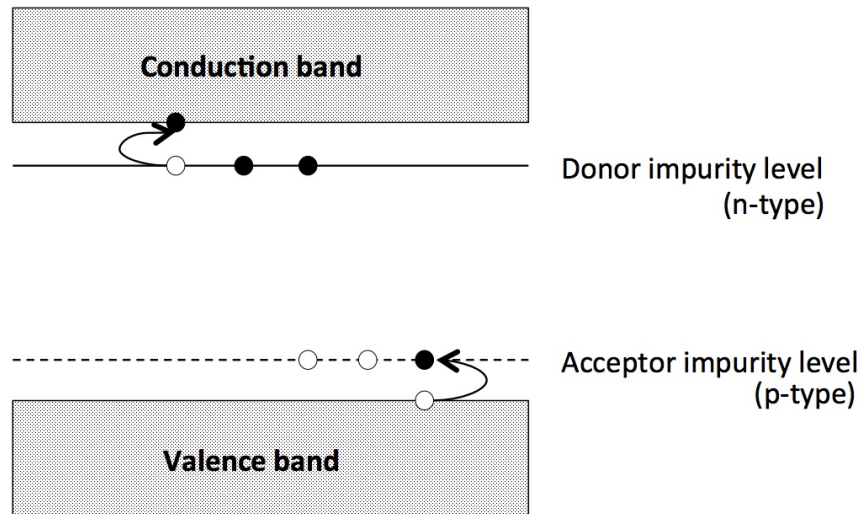


Figure 15: Schematic diagram representing the presence of dopants/impurities in a semiconductor which provide accessible levels close to the conduction and valence bands. Reproduced from source³⁷.

As previously mentioned, a sought-after property of diamond is its negative electron affinity (NEA)⁴¹, present when the diamond surface is hydrogen-terminated. In order for a surface to possess an NEA it must have its CBM above the vacuum level i.e. electrons can easily escape the material. Whereas the workfunction (ϕ) of a material is described as the energy required to remove an electron from the bulk (Fermi level, (E_F)) to infinity (vacuum level (E_{vac})), electron affinity (χ) is measured from the CBM to the vacuum level, as depicted below.

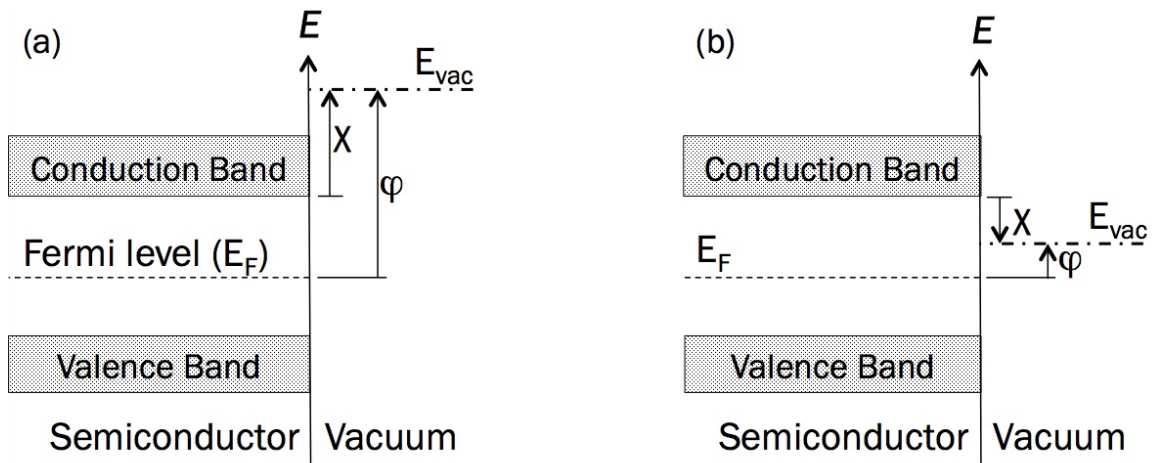


Figure 16: Simplified band theory depictions of measuring the work function (ϕ) and the electron affinity (χ) of (a) a positive electron affinity (PEA) and (b) a NEA semi-conducting material.

Reproduced from source ^[37]

It is essential here to distinguish the difference between the two different NEA models: true NEA and effective NEA. In the diagram below (Fig. 17) we can acknowledge the presence of surface-state-induced band bending, a phenomenon common to semiconductors⁴². The example given is for a classic p-type semiconductor (i.e. BDD) where electrons flow from the surface to the bulk causing downwards band-bending; as holes are repulsed from the surface a depletion layer forms.

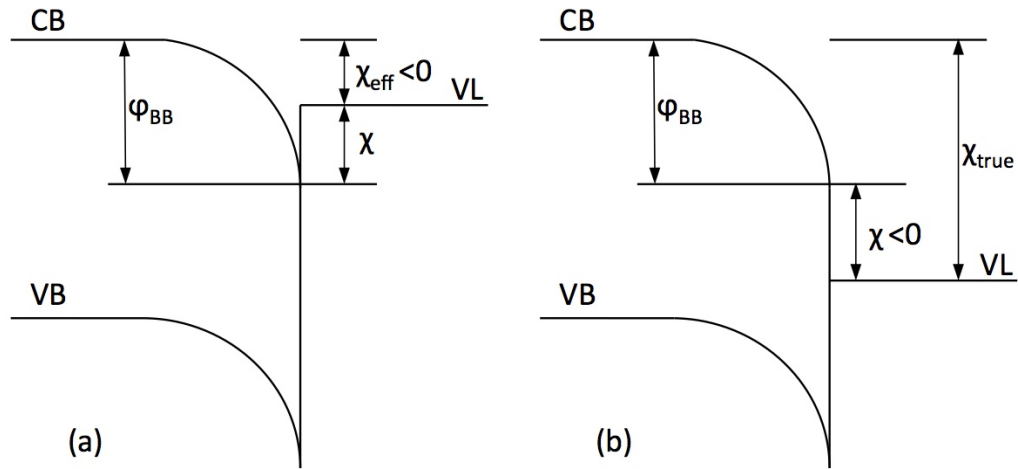


Figure 17: Band theory diagram showing the effect of band bending at a p-type semiconductor surface for (a) an effective NEA and (b) a true NEA. VB, CB and VL are the valence band, conduction band and vacuum level, respectively, whilst ϕ_{BB} represents band bending. Reproduced from source⁴³

van der Weide *et al.* demonstrated that NEA can also be established as a result of lowering the dipole barrier at the diamond surface⁴⁴. Krainsky *et al.*⁴³ laid testament to this fact through showing how increasing the amount of hydrogen-termination on a CVD-grown diamond surface could change the surface NEA from effective to true.

Important applications of diamond NEA are found in electron emission devices like photocathodes, cold-cathode emitters and thermionic energy conversion devices (TECs)⁴⁵. The latter of these applications harnesses thermionic emission, which is useful for its application in electricity generation through the conversion of heat to electrical work. In thermionic emission, heating a substrate (the emitter) in vacuum provides electrons with enough energy to overcome the workfunction (ϕ) of the material, which leads to their ejection. An equal and opposite charge remains in the material, however if the ejected electrons are captured on another cooler nearby

electrode (the collector), and the two electrodes are connected together to complete the circuit, electrons will flow driven solely by the heat difference between the emitter and collector. As can be understood by Fig. 17(b), semiconductors possessing a true NEA as with diamond could emit electrons in to the vacuum level once electrons have accessed the CBM through thermal excitation.

An oxygen-terminated diamond surface actually possesses a positive electron affinity⁴⁶ however promising research shows fine-tuning of the NEA surface is capable through varying surface treatments^{47, 48}. Loh *et al.*⁴⁷ showed that annealing/oxidation followed by caesiation (caesium deposition) restores diamond surface NEA after oxidation of the diamond surface. In this way the stability of the diamond surface is greatly improved, offsetting thermal decomposition of the chemisorbed surface elements to 650K. A later study by Geiss *et al.*⁴⁸ also found caesiation effectively provides a NEA thin film surface on doped polycrystalline diamond.

3. Instrumentation and Techniques

3.1. CVD diamond growth

3.1.1. Instrumentation

The first step of experimentation required that consistent replications of polycrystalline diamond surfaces were grown as a base to allow further manipulation. Diamond synthesis was undertaken with the use of a custom-made HFCVD reactor available in the University of Bristol Diamond Lab. The set-up was as depicted below.

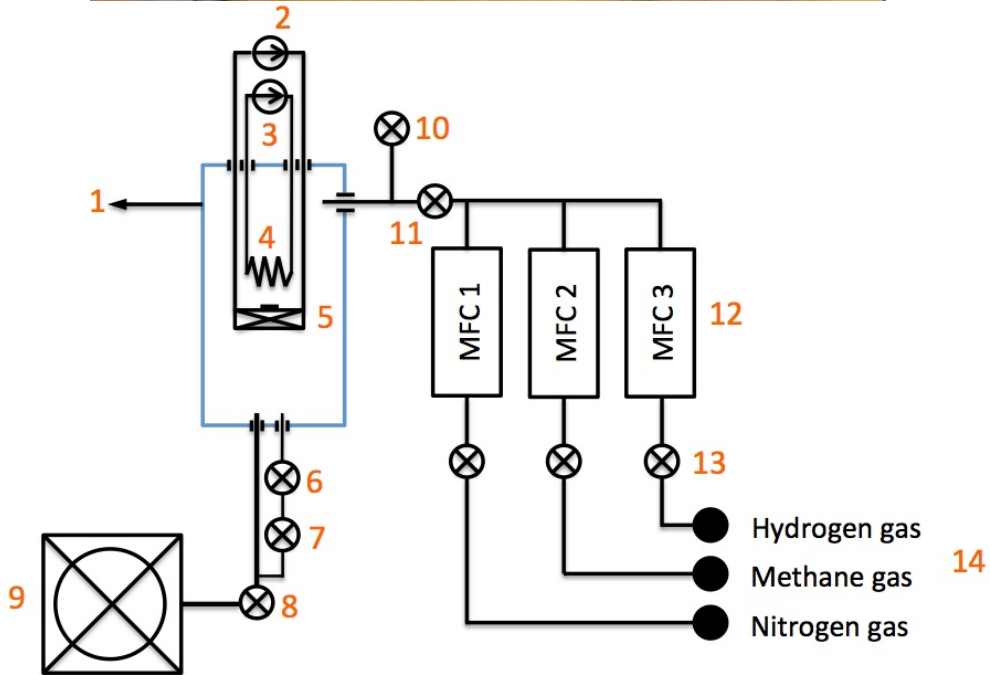
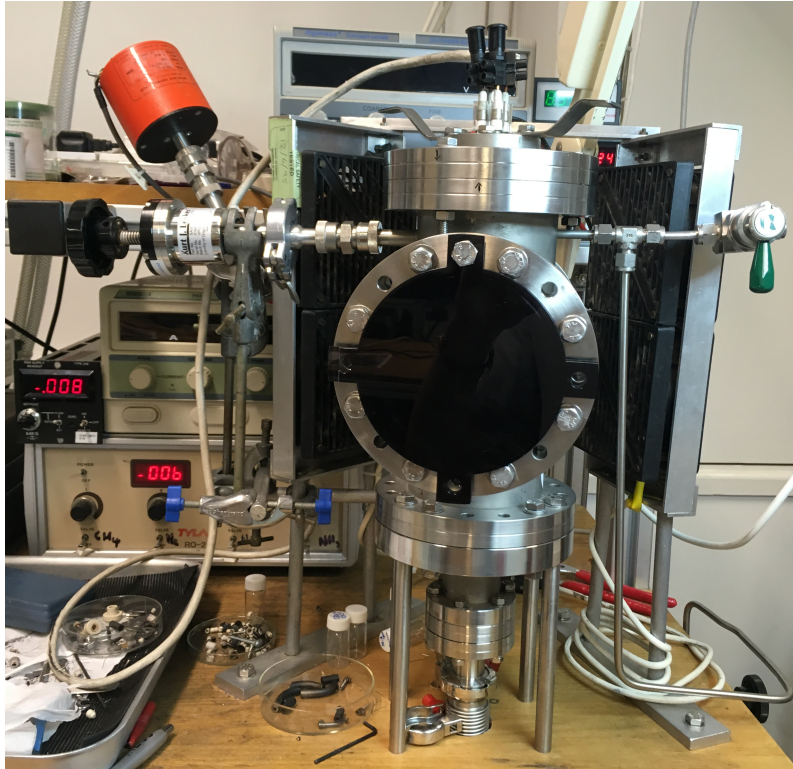


Figure 18 – Photograph (above) and schematic diagram (below) of HFCVD reactor at University of Bristol. Components in the schematic are: 1 – to pressure gauges; 2 - filament power supply; 3 - heater power supply; 4 - filament; 5 - sample stage and heater; 6 - needle valve; 7 - butterfly valve; 8 - shut-off valve; 9 - rotary pump; 10 - vent; 11 - gas inlet valve; 12 - mass flow controllers 1 to 3; 13 - on/off valves 1 to 3; 14 - gas cylinders.

Thus the reactor consists of three main components (Fig. 18); gas feed, reaction chamber and process gas removal. Starting with the gas feed: methane, hydrogen and nitrogen were stored in gas cylinders in an adjacent gas storage room, all of which were brought in to proximity of the reactor through stainless steel piping. Hydrogen gas (Air Liquide, CP grade, 99.995%), methane gas (BOC, Research grade, 99.99%) and nitrogen gas (BOC, OFN, CP grade, 99.99%) was fed to the mass flow controllers (MFC 1 to 3) where they could be fed in to the reaction chamber itself through the gas inlet pipe. Each gas was fed through its individual MFC and was calibrated relative to N₂ via the relevant gas correction factor.

The reaction chamber itself was constructed from stainless steel and has been marked out in blue, centre left of the schematic diagram. Said chamber is static bar a removable lid from which descends the sample stage (Fig. 19) allowing the sample to be inserted and subsequently suspended in the chamber by stainless steel rods extending from the underside of the reactor lid. The substrate then sat atop a platform which was heated from underneath. Hence the DC bench power supply (HQ-Power, PS3010) connected to the substrate heater, again through the detachable lid segment, using wires protected from carburization by ceramic bead coverage. It was previously found using a thermocouple that the heater reaches 400°C in the absence of filament heat.

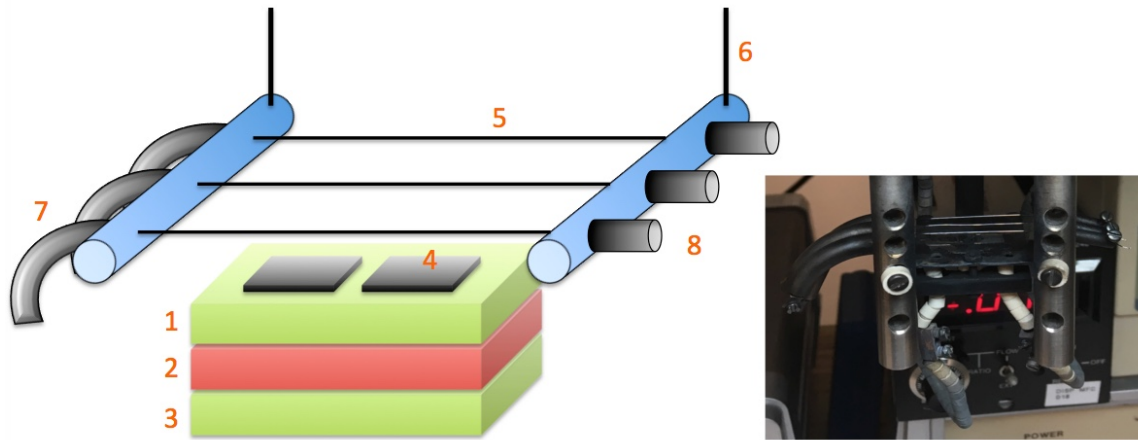


Figure 19: Photograph (right) and schematic diagram (left) of the suspended platform in the HFCVD reaction chamber. Labelled components are 1 - molybdenum top-plate; 2 - substrate heater; 3 - stainless steel underside; 4 - substrate; 5 - filament wires; 6 - power supply connections; 7 - spring-loaded wire grips; 8 - wire grips

Power was supplied to the filament in a similar manner from another DC bench supply (Digimess, SM3040). The 3 manually fitted filament wires were made of tantalum (Ta) (Advent Research Material Ltd, 99.9% purity, 0.25 mm diameter) or rhenium (Re) (Goodfellow, 99.97% purity, 0.25 mm diameter, annealed temper) and located a distance of 3 mm above the substrate. Both materials were used at different stages of experimentation. Tantalum is the cheaper material yet is suitable for one time use only as it is liable to rapid carburization, whilst rhenium filaments should last up to 3 months in the reactor with persistent use due to its superior mechanical stability⁴⁹. The filament wires were pulled taut during installation and are attached to spring loaded holders, thus in the case of rhenium filaments they can withstand the contraction and expansion endured in the reaction. The tightness of the filament wires also prevented the filament from drooping further towards the substrate where it could cause heat-damage to it.

Pressure is monitored in the reaction chamber by two pressure gauges, a capacitance manometer (Vacuum General, CMLB-21) to measure the higher pressures attained during CVD operation as well as a Pirani (Edwards, PG100-XM) to ensure a low base pressure is reached prior to reaction.

Finally the process gases were removed post-process with a rotary vacuum (Leybold Trivac D8B), which could attain a base pressure of ~ 8 mTorr. Note that the needle and butterfly valve, present along the narrower exit pipe, when used in combination allow a higher pressure of 20 Torr to be achieved during reaction. Hence exhaust gases (mainly H_2) can be removed at a slower pace than if the larger shut-off valve were open on the larger diameter outlet pipe. Thus the higher pressure of gaseous components allowed step-wise diamond growth from individual carbon-containing methane components whilst activated hydrogen prevents sp^2 graphitic carbon build-up.

3.1.2. Standard Operation

The substrate employed was p-type monocrystalline $\langle 100 \rangle$ boron-doped silicon ($\Omega = 1 - 10 \text{ ohm cm}^{-1}$), $500 \pm 25 \text{ }\mu\text{m}$ in thickness with a single side polish. The silicon was cut in to squares of size roughly 1 cm^2 using tweezers, before the polished side was seeded using manual abrasion with natural micron diamond power (Diadust®, Grade 1-3) with a median crystal size of $2 \text{ }\mu\text{m}$. Excess diamond powder was removed with ethanol. Once the samples have been prepared and dried in air they are ready for insertion on the platform of the CVD reactor. Two samples at a time could be placed on the platform to give uniform diamond growth across both. Once the filaments have been manually fitted as described previously the reactor lid and attached sample stage can be lowered in to the reactor and the lid sealed with bolts. Atop the static reaction chamber sits an elastomeric O-ring that provided an airtight

seal. Now the vent to air can be closed and the chamber pumped-down to base pressure of $\sim 8 \times 10^{-3}$ Torr. Once the vacuum had been established the substrate heater could be turned on providing a constant current of 4A for 30 minutes prior to gas intake. Next reaction gases were allowed to enter the reaction vessel, as controlled via a digital read out meter and mass flow controller (Tylan RO- 28). All diamond samples were grown using the same reaction conditions as set out here onwards, at a flow rate given in standard cubic centimetres per minute (sccm). Note that neither N_2 nor diborane (B_2H_6) were incorporated into the synthesis gas so as to give an undoped polycrystalline diamond layer.

Table 1: MFC controlled gas flow in to the reaction chamber for standard operation, as well as the gaseous composition and correction factor of the mass flow controller.

Gas	Gas Correction Factor	Gas Flow Rate / sccm	Percentage composition / %
H₂	1.00	200	99
CH₄	0.72	2	1

Once the CVD pressure of 20 Torr was achieved the filament was switched on to provide a constant current of 25A through the filament wires, reaching temperatures of ~ 2500 °C. After 7 hours of growth a polycrystalline diamond film of 2 - 3 μm is formed. To ensure the surface is hydrogen terminated, the CH_4 MFC was closed just prior to filament powering down and gas evacuation.

3.2. Scanning Electron Microscopy (SEM)

SEM was used on numerous occasions throughout this project to confirm topographical consistency across lab-grown diamond samples before and after oxygen-termination. The Department of Chemistry at the University of Bristol provides access to a range of electron microscopes, of which I chose the Jeol IT300 SEM. This system provides resolution down to a sub-nanometre scale by firing a beam of accelerated electrons treated as de Broglie particles at a sample under high vacuum. The resolution and depth of image depends on the acceleration of these electrons as shown using the following equations⁵⁰. The first gives the kinetic energy of an electron of charge, e , accelerated by a voltage, V , with mass, m , and a velocity, v .

$$\frac{1}{2}mv^2 = eV \quad (3)$$

Electron velocity is given by classical mechanics as shown:

$$v = \frac{p}{m} \quad (4)$$

And the de Broglie relationship gives momentum, p , as below (where h is Planck's constant):

$$p = \frac{h}{\lambda} \quad (5)$$

Thus finally, due to wave-particle duality the wavelength and hence resolution of electron imaging is given by the last equation:

$$\lambda = \frac{h}{\sqrt{2meV}} \quad (6)$$

Hence resolution is proportional to the inverse root of voltage. The general set-up for SEM imaging is detailed below. In essence, the electrons in the electron beam are

rastered across the sample surface with a known kinetic energy. Through inelastic scattering events, low energy secondary electrons are ejected from the sample surface and are thereafter accelerated towards a detector, where they can be amplified to give an image.

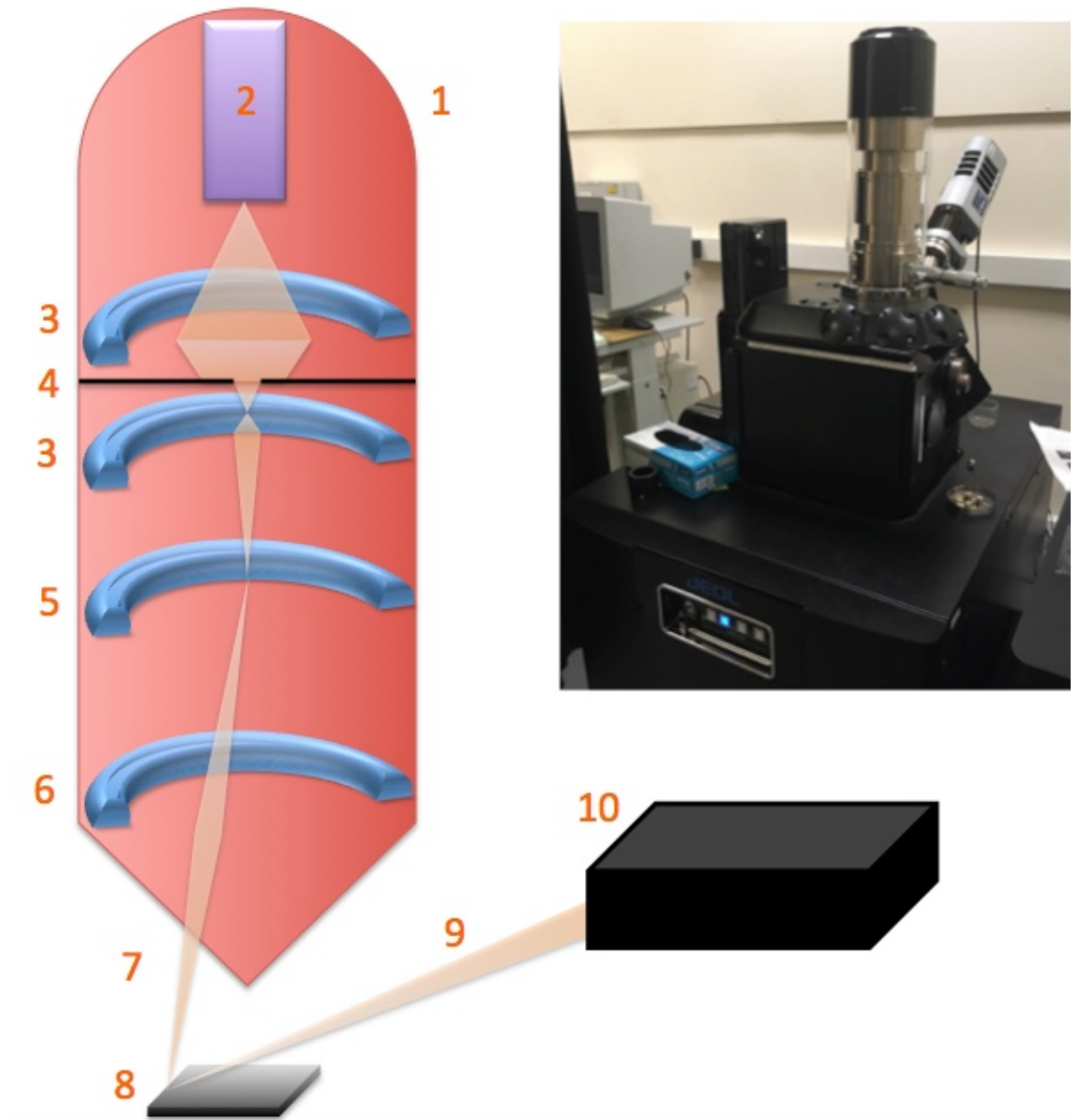


Figure 20: Photograph (top right) and schematic cross-section diagram (left) of typical SEM microscope. Latter reproduced from source^[50]. Components are 1 - vacuum chamber; 2 - electron gun; 3 - condensing lenses; 4 - aperture; 5 - rastering coils; 6 - objective lens; 7 - electron beam; 8 - sample; 9 - secondary electrons; 10 - detector.

The working distance, the distance between the objective lens and the sample surface was kept constant at around 15mm, whilst the electron beam acceleration was kept between 10-15 kV to afford good resolution and depth of image. It's noteworthy that SEM imaging is susceptible to 'charging' of non-conducting samples, where the image quality is damaged due to excessive electron build-up in the sample.

3.3. Wettability

CA measurements were frequently performed throughout my experimentation to confirm the successful oxidation of an originally H-terminated surface before and after exposure to oxygen plasma. These measurements were carried out with a Krüss Droplet Shape Analyzer (DSA) present in the Department of Chemistry, and analysis was performed using the corresponding programme as also provided by Krüss, named Advance.

All droplets placed on the sample surface were precisely 2.0 μL in volume, as provided by system automation, at a pumping rate of 0.16 mL/min. A 1mL PTFE tipped syringe was manually filled with the liquid phase prior to insertion in to the DSA. Subsequent droplet shape analysis was undertaken using the sessile drop method, as previously described, whereas the fitting method assumed the droplet to be elliptical in shape if imagined to continue in to the solid phase. The fitting method was named on the program as ellipse (tangent-1). Again this process was automated and manually confirmed through means of a direct video feed of droplet placement and subsequent spreading. The programme would give the left-hand, right-hand and mean CA, the latter being selected for all experimentation.

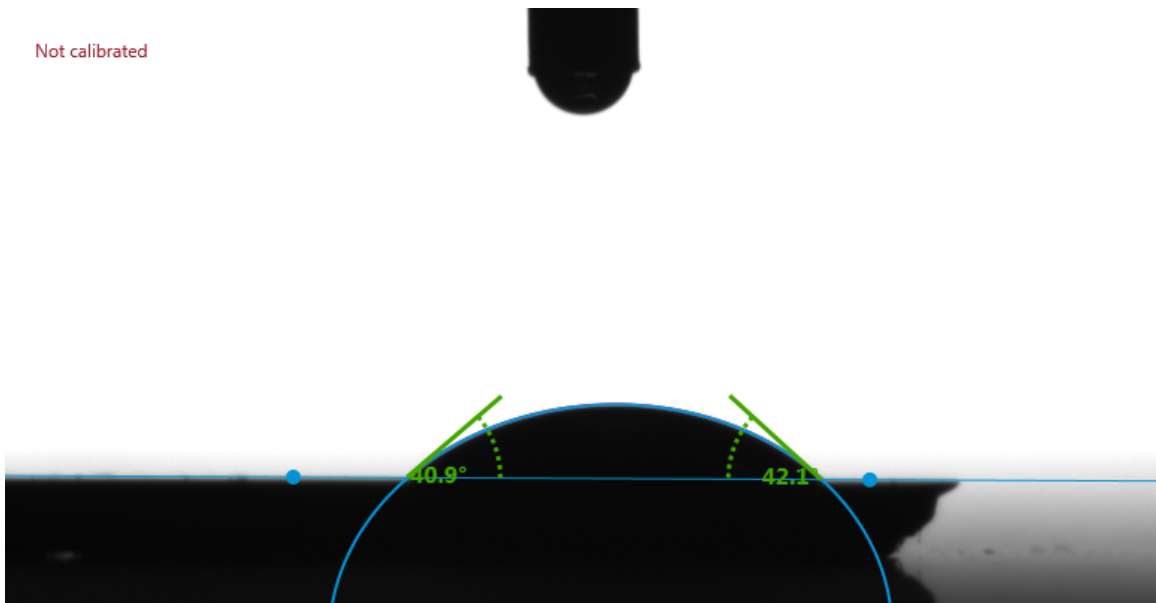


Figure 21: Photograph of a magnified water droplet on an oxidized diamond surface after 4 seconds of stabilization time. The automated ellipsoidal fitting method is displayed as well as the tangential surface-pinned intersection, allowing for left and right hand side CA measurements.

Each CA measurement was recorded precisely 4 seconds after the droplet was positioned on the surface. This was achieved by precisely setting t_0 , the time of droplet placement, using the 20 FPS video feed. The time of droplet placement was defined as when the syringe tip departs the droplet after deposition on the sample surface.



Figure 22: Photograph of the Krüss Droplet Shape Analyzer in the Krüss lab at the University of Bristol.

Prior to taking CA measurements *i.e.* placing a solvent droplet on to the diamond surface, each sample would undergo a cleaning regime where they were cleaned with water, then ethanol, and finally dried by placing them on a hotplate at 100°C for 10 minutes.

3.4. O₂ Plasma Reactor

3.4.1. Instrumentation

The O₂ plasma reactor was originally constructed for use as a sputter coater (Edwards, S150A), but after some minor modifications it was made suitable for oxygen plasma generation. Similarly to the HFCVD reactor, the O₂ plasma reactor consists of 3 main domains (Fig. 23): gas feed, reaction chamber and process gas removal.

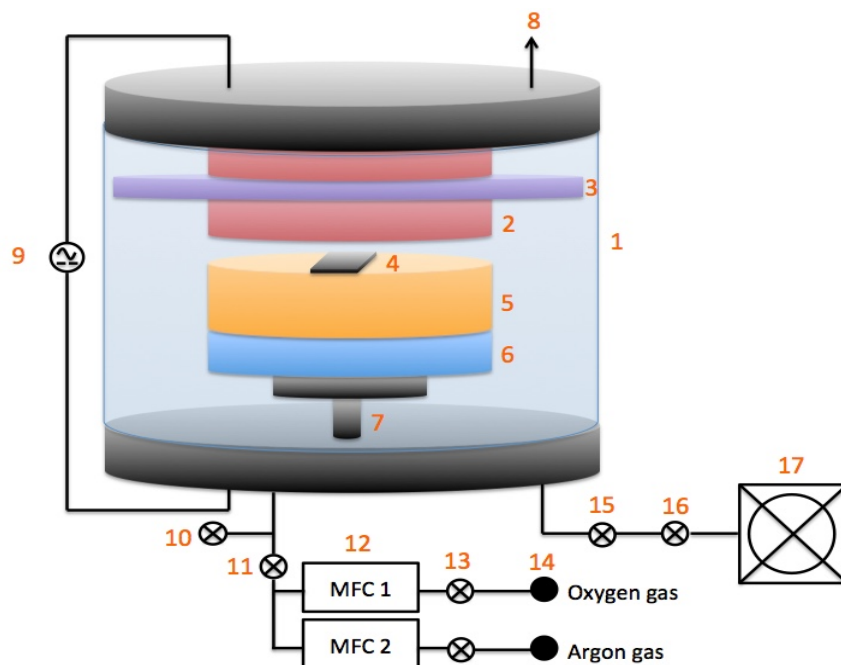


Figure 23: Photograph (above) and schematic diagram (below) of the converted sputter coater in the Department of Chemistry, now adapted for oxygen plasma formation. The labelled components are 1 – vacuum chamber; 2 – cathode; 3 – plasma shield; 4 – sample; 5 – anode; 6 – conducting layer; 7 – grounded pedestal; 8 – to pressure gauges; 9 – rectified AC power source; 10 – vent; 11 – gas inlet valve; 12 – MFC 1 and 2; 13 – on/off valves; 14 – gas cylinders; 15 – manual valve; 16 – shut-off valve; 17 – rotary pump.

As before for the HFCVD reactor, O₂ gas was brought in to proximity of the plasma reactor through stainless steel piping from the gas cylinder in an adjacent gas storage room. Two individual N₂ MFCs, each one calibrated to the traversing gas accordingly, were used to regulate the gas flow through the gas inlet in to the glass reaction chamber. Note that argon gas was not used throughout my personal experimentation through lack of necessity and that the conversion factor for O₂ is 0.993 and so the variation was deemed negligible. A rotary pump (Leybold, Trivac D10E) removed exhaust gases, as in HFCVD. Pressure within the vacuum chamber was monitored with a Pirani (Edwards, APG100) for lower pressures up to 1×10^{-4} Torr and a capacitance manometer (Baratron) for pressures of 1×10^{-1} Torr and above.

The power supply is a semi-rectified AC source, capable of achieving a voltage of 2.1 kV, which passes current from the stainless steel cathode 7 mm above the also stainless steel anode. Note underneath the stainless steel anode is a more conducting thick copper plate and that the pedestal supporting it is connected to Earth. Hence the circuit is completed only when current is passed through the gaseous oxygen, provoking the formation of a glow-discharge plasma, as characterised by the current it can carry⁵¹ which is on the order of 10^{-3} A. Furthermore the borosilicate plasma shield, helps to prevent the spread of the plasma. Carefully positioned neodymium magnets also encourage improved plasma stability, but a detailed analysis of the magnetohydrodynamics that explains this phenomenon shan't be explored here.

3.4.2. Standard Operation

Standard operation was undertaken by firstly placing a sample of hydrogen-terminated diamond, as grown using the HFCVD reactor as described above, on top of the anode before closing the vacuum chamber lid. An airtight seal was formed on closing the reaction chamber lid with the use of an O-ring. The vacuum chamber was evacuated to achieve a base pressure of $\sim 8 \times 10^{-3}$ Torr before introducing oxygen in to the chamber via a digital read-out meter and MFC (Tylan RO-28) at rate of 10 sccm.

Next, tweaking the manual valve, which leads to the rotary pump, alters the pressure within the reaction chamber. Pressure values were varied throughout my experimentation within the stable plasma range of 0.1- 1.5 Torr, for which continuous glow-discharge plasma was observed. After 2 Torr the plasma would flicker, independent of other variables including flow rate and applied potential difference, and hence setting the operational limits of the reactor.

Once a stable pressure has been established, the power supply can be turned on. The voltage must exceed the breakdown voltage necessary to form a self-sustaining glow discharge plasma as given by Paschen's law⁵². This concept is simple to understand when we consider a gas as a perfect insulator when under the influence of weak electric fields, consisting of electrically neutral and separated molecules or atoms. However once a sufficiently large electric field is present, ionisation of the gaseous molecules provoking a whole host of subsequent processes including elastic collisions, ionisation, and excitation. Hence the non-electro neutral products of this avalanche of reactions are capable of carrying a current via fast moving electrons but also the slower ions. The breakdown voltage, V_b , increases significantly with the distance, d , between the two electrodes via the relationship as shown:

$$p_0 d = \frac{V_b}{(E/p_0)} \quad (7)$$

Note that the breakdown voltage is not dependent on the distance between electrodes and the measure of the gas concentration, p_0 , separately, but is dependent on the product of the two variables. Also, although p_0 is technically a pressure it is more specifically the gas pressure at 0°C, which provides a useful measure for gas concentration. Finally, (E/p_0) defines the processes associated with electron movement in the glow discharge, where E corresponds to the electric field strength.

Paschen's law produces Paschen curves that plot V_b against $p_0 d$. Paschen curves are affected predominately by two variables: η , the ionisation coefficient and γ , the secondary emission coefficient. Both of which are related to the multiplication factor, q , by the following relationship:

$$q = \gamma(e^{\eta V_b} - 1) = 1 \quad (8)$$

The above equation describes how q , the number of additional electrons emitted from subsequent atomic or molecular interactions following the emission of a single electron from the cathode, must be equal to unity in order for the value of the current to remain constant. The ionisation coefficient depends solely on the gas and describes the likelihood that ionization of a gaseous entity will occur upon electron absorption instead of excitation or other energy loss in the form of elastic collision. Whilst the secondary emission coefficient depends upon both the gas and the cathode material as it describes the probability of a positive ion liberating additional electrons from the cathode upon contact.

Essentially we need not worry about any of the above directly in relationship to my experimentation. We need merely acknowledge that the distance between the electrodes is sufficiently short that within the operating limits of the plasma reactor, the breakdown voltage is exceeded for all voltages within the range of $\sim 0.2 - 2.1$ kV in a pure oxygen environment. Hence accordingly throughout my experimentation the voltages within this complete range were explored *vis à vis* the optimization of the plasma reactor.

The final characteristic variable of the O_2 plasma reactor was time, which was varied from 1 to 10 s. Such a small range was explored as a result of preliminary work showing that an optimal value for surface oxidation lay within this range.



Figure 24: Photographs of the O_2 plasma reactor during operation and hence displaying the self-sustaining glow discharge in the light (left) and in darkness (right).

A point of interest is the colour of the plasma, which is characteristic of a pure oxygen glow-discharge and ascertains to the release of a photon of light within the visible region of the electromagnetic spectrum when an excited O_2 molecule returns to its ground state.

3.5. Laser Raman Spectroscopy

Once diamond surfaces had been synthesised in the HFCVD reactor, Laser Raman Spectroscopy was used afterward to confirm the successful synthesis of diamond with the spectrometer available in the Diamond Lab (Renishaw 2000).



Figure 25: Photograph of the Laser Raman Spectrometer (Renishaw 2000) in the Department of Chemistry, University of Bristol.

For our purposes, I employed the 514 nm laser (Green, Ar⁺) which allowed detection of sp² impurities in the predominantly sp³ diamond lattice structure. Raman spectroscopy detects low intensity inelastic Stokes' scattering photons, emitted after the absorption of a photon of higher energy. Inelasticity occurs when the energy of the emitted photon is less than that of the originally adsorbed photo that resulted in the increase in vibrational energy level of the molecule. Anti-Stokes' Raman scattering is also possible where the energy of the photon emitted, upon the molecule returning to a lower energy vibrational level, is higher than the energy of the photon originally adsorbed. However the intensity of anti-Stokes' scattering is less than that of Stokes' scattering, thus we observe Stokes' inelastic scattering events only. The most intense scattering is from elastic Rayleigh scattering, as is usually detected in IR spectroscopy, although in Raman spectroscopy a filter is used to block out this type of emission.

For sp³ polycrystalline diamond, the most intense peak corresponding to Stokes' scattering gives a narrow peak in Raman spectroscopy at 1332 cm⁻¹ when a monochromatic 514 nm laser is used⁵³. There is a correlation between the width, or more precisely full-width half maximum (FWHM) of the 1332 cm⁻¹ peak, and the amount of sp² regions in the diamond film⁵⁴. Hence although the non-diamond carbon peaks appear in a broad range spanning from ~1100-1600 cm⁻¹, we need only analyse the sp³ peak in order to extrapolate the diamond quality.

Normal operation required centring the spectra on the sp³ diamond peak at 1332 cm⁻¹ in the program (Wire 2.0). The laser would first be calibrated to single crystal (100) diamond samples before exposing to CVD grown samples. A stretch

frequency value for each sample was collected through 10 accumulations of 1 s of laser exposure (at 10% laser power) through a 50x magnification lens.

3.6. X-ray Photoelectron Spectroscopy (XPS)

X-ray Photoelectron Spectroscopy provides quantitative analysis of surface composition up to 10 nm deep and can be carried out here at Bristol at the NanoESCA facility in the Centre for Nanoscience and Quantum Information (NSQI) building, where ESCA stands for Electron Spectroscopy for Chemical Analysis. Soft monochromatic Al K_{α} X-rays, of energy 1486.7 eV, cause photoionization of core electrons allowing analysis of the kinetic energy of emitted photoelectrons⁵⁵. A surface atom, A , absorbs the high energy X-ray, $h\nu$, and is ionized in the process:



Conservation of energy requires that the energy of the atom interacting with the X-ray is equivalent to that of the ion, A^+ , plus the emitted electron, e^- :

$$E(A) + h\nu = E(A^+) + E(e^-) \quad (10)$$

Hence through inelastic photoionization the energy of the departing photoelectron can be considered solely as kinetic energy, KE :

$$KE = h\nu - (E(A^+) - E(A)) \quad (11)$$

The final bracketed term, representing the difference in energy between ionized and neutral atoms is called the binding energy, BE , of the electron, which gives us the final most commonly quoted equation:

$$KE = h\nu - BE \quad (12)$$

These binding energies are characteristic for any core electron of any element, and as such peaks can be identified and assigned accordingly. Elastic photoemission gives discrete peaks corresponding to the shell structure of atomic electrons, whilst inelastic photoemission gives rise to noisy background. Closer analysis of the discrete peaks stemming from elastic photoemission reveals chemically shifted peaks, much as in NMR spectroscopy. These chemically shifted peaks arise from a difference in binding energy of core electrons, dependent on two factors: oxidation state of the atom and local chemical and physical environment. Many tabulations of chemical shift exist, yet measurements appear to be inconsistent across instruments, moreover it is the difference in binding energy, ΔBE , which remains constant⁵⁶.

A standard and simplified XPS system is depicted below:

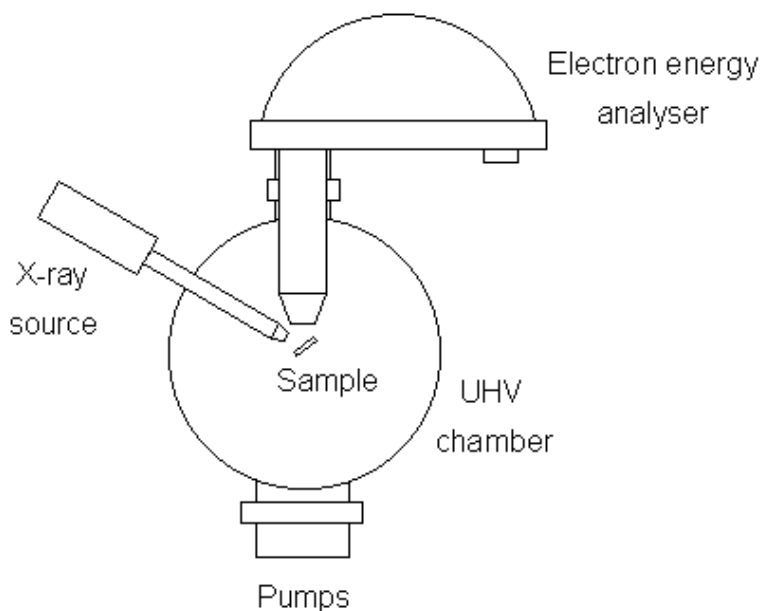


Figure 26 : Typical set-up for XPS analysis, as in the NanoESCA facility in the NSQI building at the University of Bristol.

Like with many ESCA techniques, an ultra-high vacuum (UHV) is required to maximise surface sensitivity by way of removing interfering gas phase particles. The NanoESCA facility in Bristol is fitted with a hemispherical ARGUS electron energy analyser that permits a maximum energy resolution of less than 300 meV. The sample was orientated at 84° to this detector, thus determining the take off angle which dictates the information depth (ID)⁵⁷.

4. Experimental Method

4.1. Preliminary Investigation

Samples of hydrogen-terminated diamond were grown on silicon wafer substrates to a thickness of between 2 and 3 µm in the HFCVD reactor, following the procedure for standard CVD operation as described previously. The growth time was kept constant at 7 hours in which time the filament would remain on. Once nine samples had been grown, sp³ diamond presence and quality was analysed using Laser Raman Spectroscopy and topographical continuity was verified using SEM. Nine hydrogen-terminated samples were subjected to exposure to the O₂ plasma in the O₂ plasma reactor for varying amounts of time, being 0, 3, 4, 5, 6, 7, 8, 9 and 10 seconds. All other parameters were kept constant during this time, with the values as shown below.

Table 2: Controlled variables for the investigation of time varied oxygen-termination using the O₂ plasma reactor.

Parameter	Value
Pressure / Torr	0.7
Voltage / kV	1.35

Flow rate was also kept constant, as described previously, at 10 sccm of pure O₂. All samples had their CA measured, prior to oxygen-termination, for the hydrogen-terminated surfaces using water as a liquid phase. CAs were then recorded post O₂ plasma treatment, again using water as a liquid phase. CA measurements using water were then repeated twice more after fortnightly intervals, again after being subjected to the cleaning regime prior to measurement. After the first fortnight since the initial measurements were taken, only the 0, 3 and 4 second O-terminated samples were re-measured. Four weeks after the initial measurements, CA measurements for all samples were repeated.

4.2. Surface free energy (SFE) calculation

Measurements of CA were taken for each of the diamond surfaces that were analysed in the preliminary investigation *i.e.* those oxidized in the plasma reactor for 0, 3, 4, 5, 6, 7, 8, 9 and 10 seconds. For each different liquid phase (ethylene glycol, distilled water and diiodomethane) a single droplet, of 2 μ L in volume, was placed in the centre of the surface to provide the CA for that particular liquid phase. Between measurements with a different solvent, the sample was cleaned using water, then ethanol before finally drying, as described previously.

4.3. Taguchi Optimization

Prior to commencing the Taguchi analysis, the necessary methodology⁵⁸ to undertake the procedure was observed. Offline quality control for process design improvement requires identification of signal, noise and control factors. Signal factors are those that improve product quality whilst bringing the mean response towards the target level. Noise factors produce variation in quality through

specification, and hence need minimising. The effect of control factors is also sought to be minimized, who affect the variability of a response.

For complete Taguchi analysis, 16 polycrystalline diamond samples were grown, again using the standard procedure for HFCVD diamond growth as outlined previously. Once the diamond samples were obtained, each sample was oxidized using the O₂ plasma reactor, but for each run the parameters were ran at different levels, in accordance with the P = 3, L = 4 L₁₆ Orthogonal Array (L₁₆ OA) as depicted below (Table 3). P here refers to the number of varied parameters whilst L refers to the number of different values (levels) used for each parameter:

Table 3: P = 3, L = 4 Taguchi Orthogonal Array displaying which level for each parameter should be used for each run. Note that the quoted numbers for pressure, voltage and time correspond to levels and not exact values. Each level is detailed in the following table (Table 4).

Run (<i>j</i>)	Pressure (P_L)	Voltage (V_L)	Time (t_L)
1	1	1	1
2	1	2	2
3	1	3	3
4	1	4	4
5	2	1	2
6	2	2	1
7	2	3	4
8	2	4	3
9	3	1	3
10	3	2	4
11	3	3	1
12	3	4	2
13	4	1	4
14	4	2	3
15	4	3	2
16	4	4	1

The corresponding values for each parameter are detailed below (Table 4):

Table 4: The values for each level in the Taguchi orthogonal array, with associated units displayed in the column headers.

Level (<i>L</i>)	Pressure (<i>P</i>) / Torr	Voltage (<i>V</i>) / kV	Time (<i>t</i>) / s
1	1.5	1.93	10
2	1.0	1.54	8
3	0.5	1.35	6
4	0.1	1.16	4

Hence for each run the orthogonal array dictates the reaction conditions under which each should be performed. Furthermore, the sample to be used for each run was randomly selected using a random number generator. To give an example, the 13th run involved placing a randomly selected H-terminated CVD diamond sample in the O₂ plasma reactor. In order to oxidize the sample, the pressure in the reaction chamber was 0.1 Torr, the voltage applied across electrodes was 1.93 kV and the voltage was applied for 4 seconds.

After all 16 samples had been oxidized in the plasma reactor according to the Taguchi matrix, 4 CAs were measured for each oxygen-terminated diamond sample following the procedure as outlined previously. Water droplets of 2 μ L in volume were deposited in each of the four corners of the roughly 1 cm² surface.

Following statistical analysis of the CAs for each sample, with a smaller-the-better (S-type) tolerance loss function⁵⁹, the optimal values for pressure, voltage and time were obtained. Seeing as a CVD grown diamond surface had not previously been modified with the O₂ plasma reactor under these exact conditions, a further diamond sample was modified in line with the results of the Taguchi optimization.

Again, this final sample underwent the same wettability analysis as all other samples for the Taguchi optimization.

4.4. XPS

Five samples were submitted to XPS analysis, which were the unmodified H-terminated as-grown CVD diamond sample (0 second O-termination), the 4, 5 and 10-second O-terminated samples from the preliminary investigation, and finally the sample that was modified in accordance with the Taguchi optimization findings. Prior to XPS analysis, each sample was individually loaded in to the UHV reaction chamber, where they were heated to 300°C for 30 minutes to remove any physisorbed surface adsorbates.

Three scanning modes were used for each sample: a survey scan, O1s scan and a C1s scan. The survey scan covered the whole energy range of binding energies from 250 – 600 eV, whilst the C 1s and O1s scans were centred around the carbon and oxygen 1s electron binding energies as produced from Al X-Rays, where the line positions are 287 and 531 eV, respectively⁶⁰. Data analysis was subsequently undertaken using the program Casa XPS.

All curve fitting of photoelectron spectra was undertaken by subtracting a Shirley background to identify and separate the overlapping contributions present within a specific BE region, corresponding to the same element present in multiple environments. When peak fitting components we aimed to reduce the residual standard deviation (Residual STD) to an acceptably low value of ≤ 5 . In order to ensure chemical and physical validity, constraints were evoked on the peaks once peak asymmetry had been accounted for, namely that the FWHM for all components

must be equal. Furthermore, the Gaussian or Lorentzian nature of the peak was adjusted to again reduce the Residual STD. The presence of both forms stems from instrument broadening effects (Gaussian) as well as the uncertainty principle associated with core hole lifetime (Lorentzian)⁶¹.

5. Results
5.1. SEM

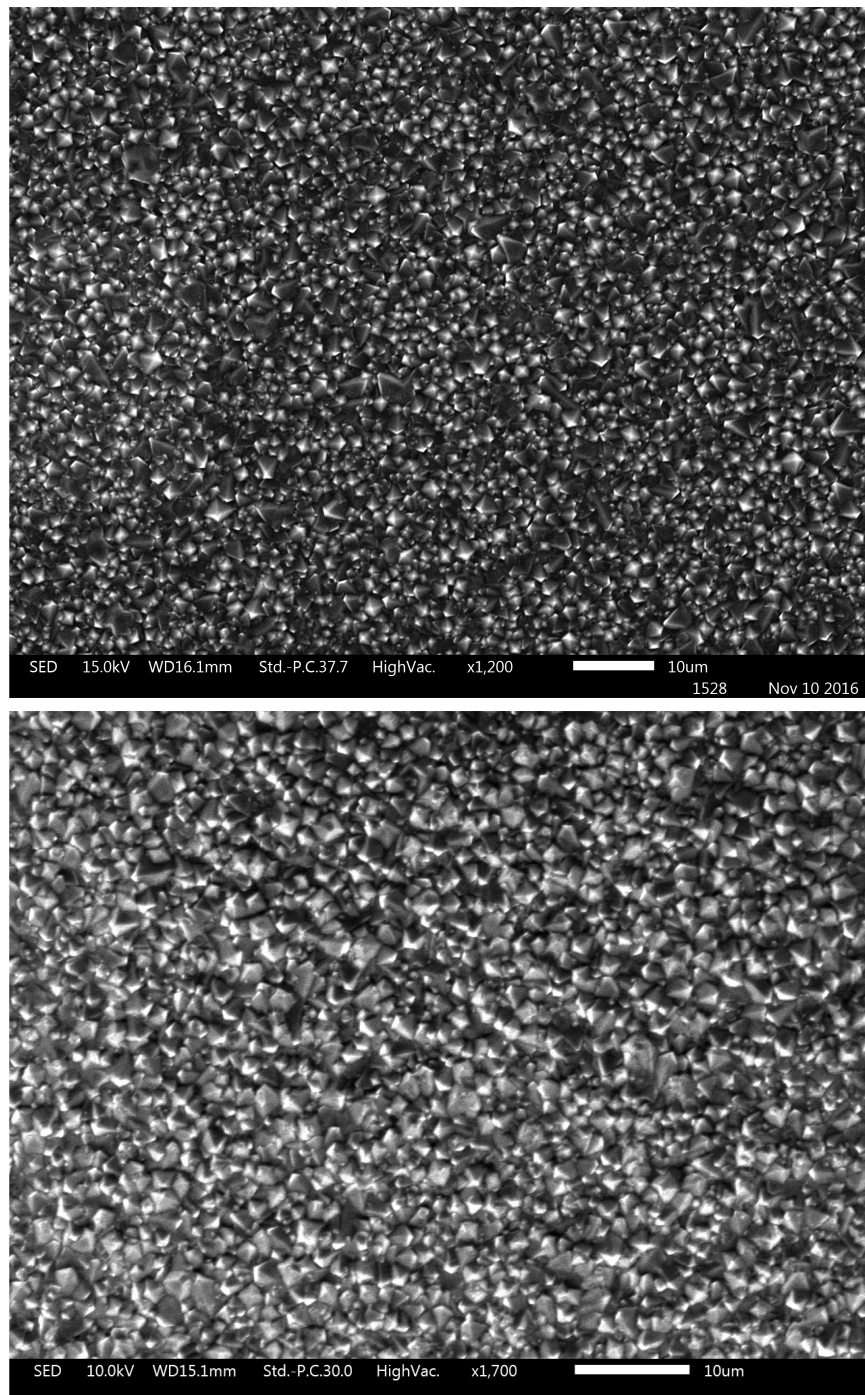


Figure 27: SEM images of the same sample pre-oxidation (above) and post-oxidation (below). Note scale bars, magnification factors and electron beam energy are discontinuous across images.

The above micrograph (Fig. 27) images depict the same diamond surface grown with HFCVD, before and after oxidation in the O₂ plasma reactor. SEM microscopy was used here in a qualitative manner to confirm the absence of surface reconstruction upon O₂ plasma treatment. A transverse SEM micrograph (Fig. 28) of a H-terminated sample was also examined to confirm the growth rate of the diamond film, which was found to be 0.35 μm h⁻¹, where films produced were ~2.4 μm thick.

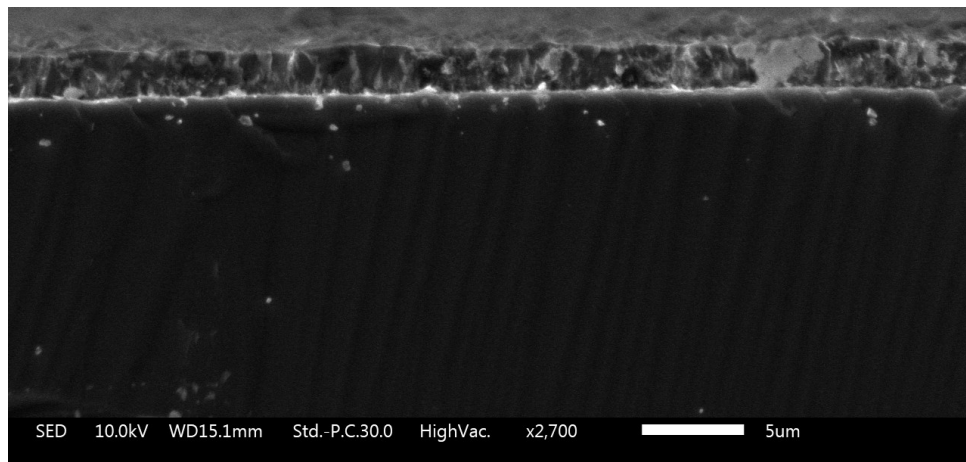


Figure 28: Transverse SEM micrograph of a H-terminated CVD diamond sample with a 2.4 μm thick diamond layer. The lower darker region of the image is the supporting Si wafer, which sits below the diamond film.

5.2. Laser Raman Spectroscopy

Raman spectroscopy was used in a purely qualitative manner to confirm diamond growth of similar quality across all samples. The sp³ diamond peak was identified for all examined samples at a position of 1333.04 ± 0.15 cm⁻¹, with a FWHM of 9.126 ± 0.281 cm⁻¹. Single crystal <100> diamond samples were also examined as

acquired, which were found to have a mean peak position at $1333.42 \pm 0.06 \text{ cm}^{-1}$ and an associated mean FWHM of $6.948 \pm 0.355 \text{ cm}^{-1}$.

The calculated error was given by the standard deviation for a population function in Excel (STDEV.P), given by the equation below. This functional form was used consistently throughout my experimentation.

$$\sigma = \sqrt{\frac{\sum(x - \bar{x})^2}{n}} \quad (13)$$

Here σ defines the standard deviation, x is the value of each CA measurement, \bar{x} is the mean CA measurement and n is the population size.

5.3. Preliminary investigation

In early preliminary work, oxygen-termination time was varied solely whilst all other variables of the O_2 plasma reactor were kept constant. The conditions originally selected were based on other preceding work that was carried out by a former student.

CAs for H-terminated surfaces and found to vary significantly, giving an average of $81.4 \pm 6.0^\circ$ across 32 measurements. The CAs for water deposition on the oxygen-terminated samples were as shown (Table 5):

Table 5: Contact angle variation for a water liquid phase against the oxygen-termination time for each diamond surface, alongside the associated error calculated across 4 measurements for each surface.

Oxygen-termination time /s	Mean contact angle/ °	Standard deviation / °
0	81.4	6.0
3	71.1	0.6
4	55.6	0.8
5	48.6	0.4
6	47.9	1.5
7	42.0	3.2
8	42.7	2.9
9	50.5	0.
10	53.8	0.9

The above CAs correspond to the initial CA measurements and are redisplayed in graphical form (Fig. 29). Alongside the initial CA measurements are those re-measured after 2 fortnightly periods.

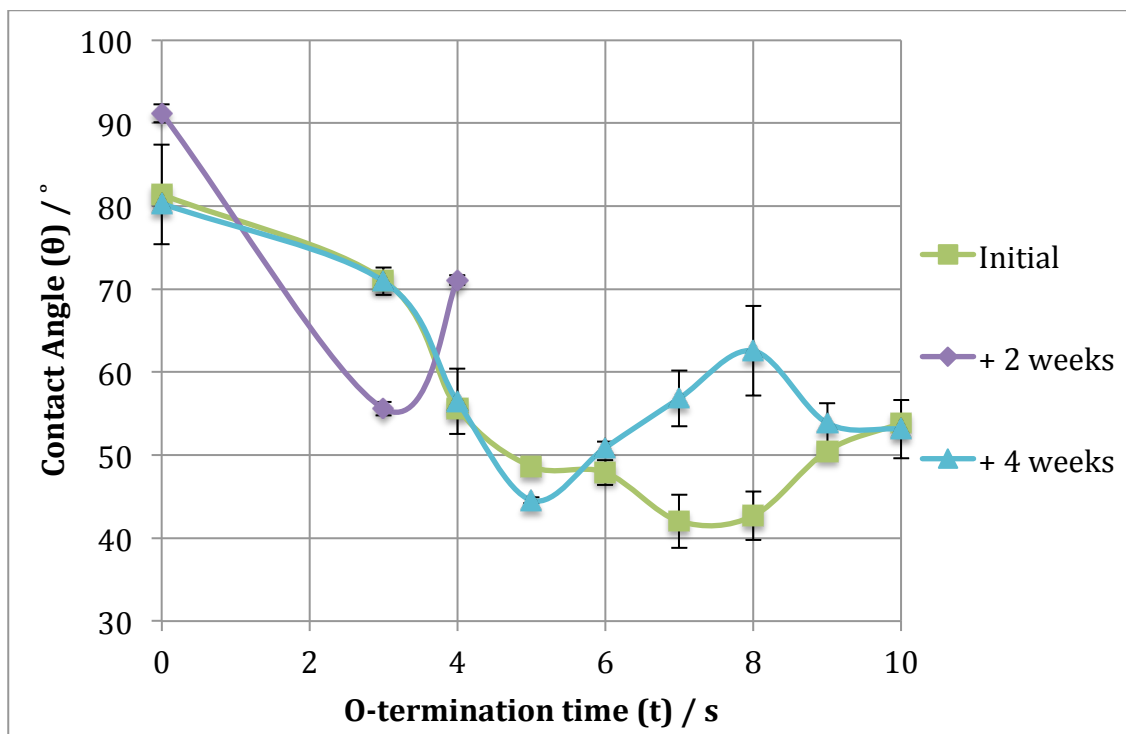


Figure 29: Graph showing the measurements of mean contact angle, with water as the liquid phase, against the time each hydrogen-terminated sample spent exposed to the oxygen plasma. Measurements were repeated after fortnightly intervals

The time averaged CA measurements are redisplayed below (Fig. 30).

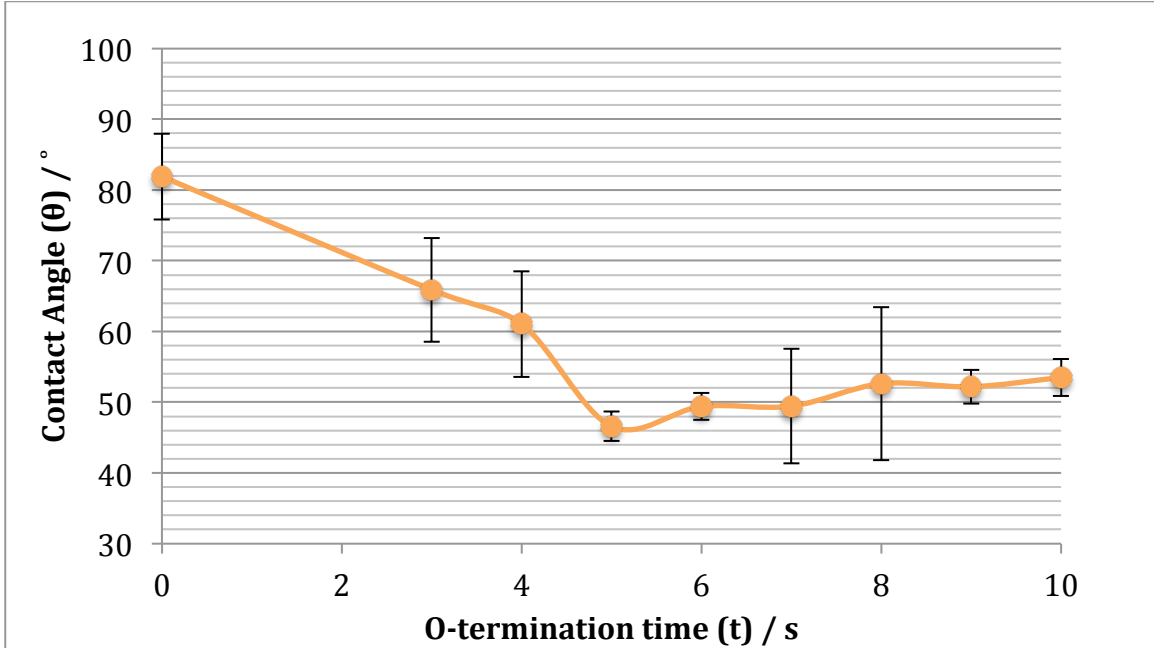


Figure 30: Average CA measurement as taken over a one month period against the time each diamond sample spent exposed to the oxygen plasma in the reactor.

5.4. SFE calculation

Derived from Fowke's equation (Equation 1) is the Owens-Wendt graphical method for determining the polar and dispersed components of a solid phase, using CA measurements with different liquid phases. The Owens-Wendt method requires fitting the data to a straight-line plot of the form $y = mx + c$, via a rearrangement of the Fowke's equation as shown:

$$\frac{\gamma_{lv}(1 + \cos \theta)}{2\sqrt{\gamma_{lv}^d}} = \sqrt{\gamma_{sv}^p} \cdot \sqrt{\frac{\gamma_{lv}^p}{\gamma_{lv}^d}} + \sqrt{\gamma_{sv}^d} \quad (14)$$

Thus on varying the solvent, the values of γ_{lv} , γ_{lv}^d , γ_{lv}^p and θ vary also, and hence γ_{sv}^p and γ_{sv}^d can be found. The liquid phase polar and dispersed components, where the polar component somewhat correlates to the dielectric constant of solvents, were

provided in the ADVANCE program database. All values are given below (Table 6) for when the temperature is 20°C and with air as the vapour phase.

Table 6: Total SFE values of various solvents used as a liquid phase in wettability measurements, separated in to their polar and disperse components.

Solvent	SFE dispersed component (γ_{lv}^d) / mNm ⁻¹	SFE polar component (γ_{lv}^p) / mNm ⁻¹	Total SFE (γ_{lv}) / mNm ⁻¹
Diiodomethane	50.8	-	50.8
Water	21.8	51.0	72.8
Ethylene glycol	26.4	21.3	47.7

Thus with 3 CA measurements from 3 different liquid phases, a linear plot of the kind shown below (Fig. 31) can be constructed.

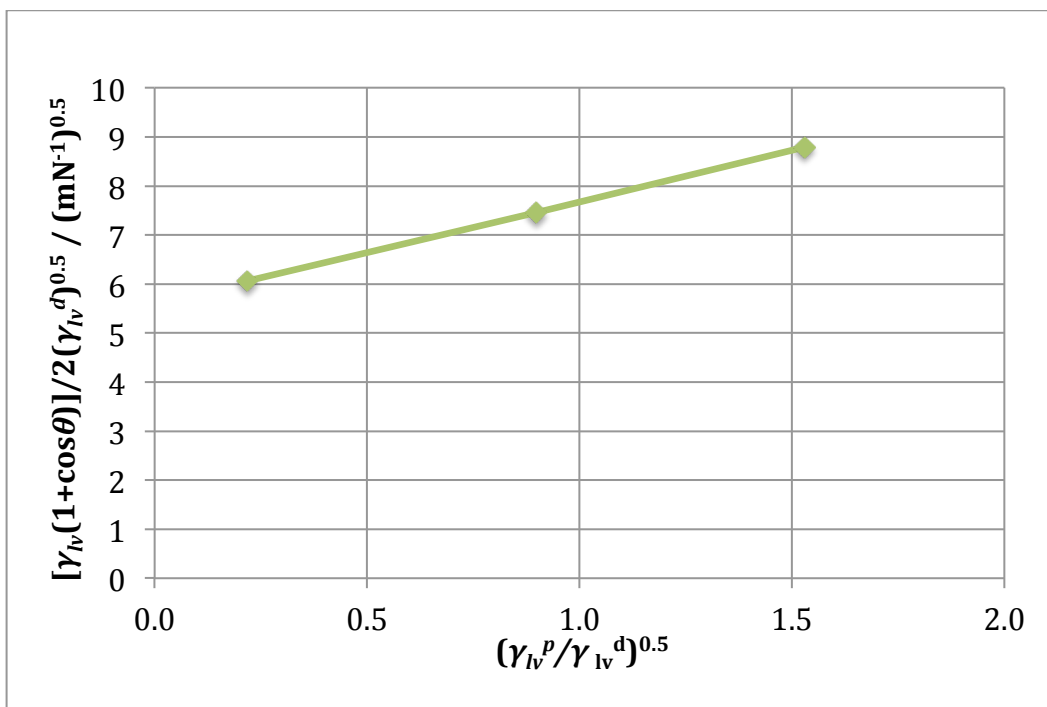


Figure 31: Straight line plot showing the Owens-Wendt method for SFE calculation where the 3 points correspond to the 3 different liquid phases used to give CA measurements. The example given is for the hydrogen-terminated sample *i.e.* 0-termination time of 0 seconds.

From the trend-line of these plots we can extrapolate the y-intercept, c , and obtain the gradient, m , in order to arrive at the contributions made to the SFE from the polar and dispersed components of the hydrogen- or oxygen-terminated diamond surfaces (Table 7).

Table 7: Values for the SFE of all samples that were oxidized in the preliminary investigation, as derived from the Owens-Wendt method.

O-termination time / s	$\gamma_{sv}^d / \text{mNm}^{-1}$	$\gamma_{sv}^p / \text{mNm}^{-1}$	$\gamma_{sv} / \text{mNm}^{-1}$
0	31.4	4.3	35.7
3	31.9	9.8	41.6
4	24.1	24.1	48.2
5	23.4	33.0	56.5
6	23.5	23.0	46.4
7	24.3	21.7	46.0
8	24.7	20.9	45.6
9	23.9	23.6	47.6
10	22.3	22.8	45.2

Note that the total SFE for the solid phase (and all phases) is simply the sum of the dispersed and polar SFE contributions:

$$\gamma_{ij} = \gamma_{ij}^d + \gamma_{ij}^p \quad (15)$$

Finally, plotting the findings gives the following graph (Fig. 32):

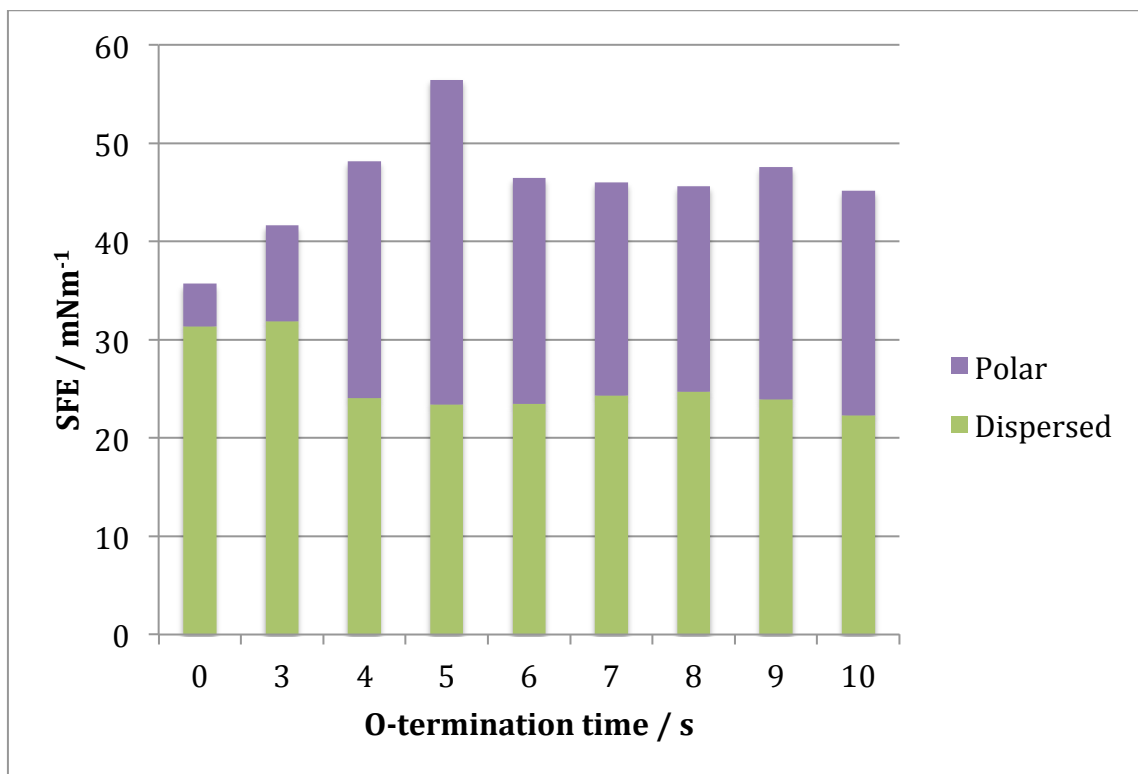


Figure 32: Total SFE separated in to the corresponding polar and dispersed contributions for each oxidized sample of the investigation.

5.5. Taguchi Optimization

Firstly, four CAs were taken on each corner of the O-terminated diamond surfaces, as oxidized according to the Taguchi orthogonal array, using water as the liquid phase. The mean CA measurements for each run have been collated below (Table 8), alongside the standard deviation across the 4 measurements.

Table 8: Mean CA measurements and associated errors for each oxygen-terminated sample, as oxidized following the outlined Taguchi orthogonal array parameters and levels. Signal-to-noise ratios (S/N ratios) are also shown as required for a Taguchi analysis.

Run (<i>j</i>)	Mean contact angle / °	Error / °	Signal to noise ratio (η_j) /dB
1	68.1	1.18	-32.69
2	62.7	3.14	-31.97
3	52.5	1.35	-30.43
4	45.1	5.86	-29.17
5	61.6	4.19	-31.83
6	49.8	5.02	-30.01
7	63.6	5.58	-32.12
8	48.0	7.13	-29.74
9	47.8	0.85	-29.61
10	42.6	7.08	-28.73
11	56.6	13.21	-31.31
12	47.1	2.25	-29.49
13	44.1	2.62	-28.93
14	45.5	4.05	-29.21
15	45.4	2.48	-29.17
16	38.9	0.70	-27.82

A signal-to-noise ratio, η_j , was calculated for each of the 16 experiments using the following smaller-the-better (S-type) equation, seeing as we seek the smallest contact angle aligning with the most successfully oxidized surface. The sample size is denoted n whilst y refers to the CA measurement.

$$\eta_j = -10 \log_{10} \left(\frac{1}{n} \sum_{i=1}^n y_i^2 \right) \quad (16)$$

Then for each level of each variable, a summation is calculated across all experiments with the same level for a particular parameter (Table 9). An average signal-to-noise (S/N) ratio for a particular level of a variable can be calculated from this summation by dividing through by the number of runs carried out at that level, n . An example equation is shown below to give the average signal to noise ratio across all runs carried out where the pressure in the reactor was that of the first level ($L = 1$) *i.e.* 1.5 Torr.

$$S_{P=1} = \frac{\sum_{j=1}^4 \eta_j}{n} \quad (17)$$

Table 9: Average S/N ratios ($S_{P=L}$) for each level of each parameter altered in the optimization of the O₂ plasma reactor.

Level (L)	$S_{P=L}$ / dB	$S_{V=L}$ / dB	$S_{t=L}$ / dB
1	-31.07	-30.76	-30.46
2	-30.92	-29.98	-30.61
3	-29.78	-30.76	-29.75
4	-28.78	-29.06	-29.74

Eventually plotting these average S/N ratios ($S_{P=L}$) against level, as shown (Fig. 33), produces graphs. The theoretical optimal values for reaction conditions have the least negative values.

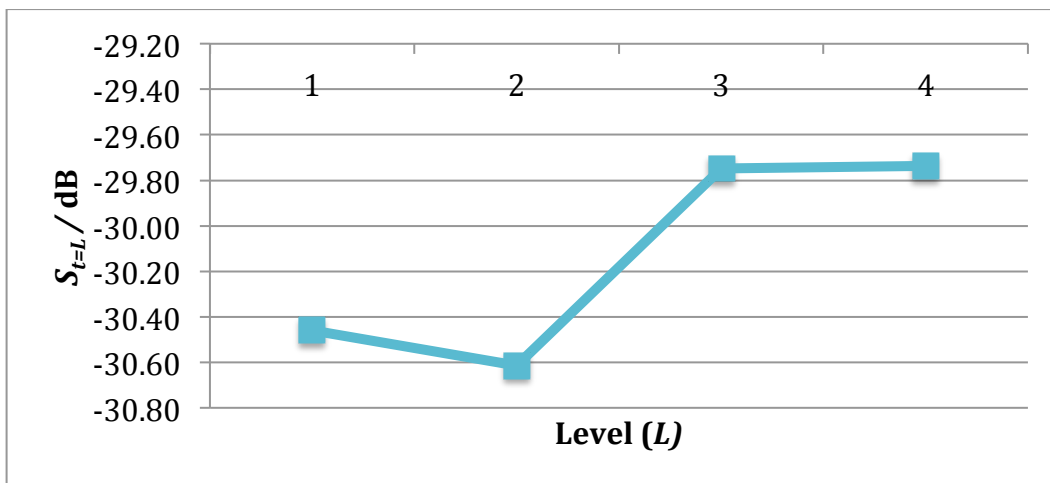
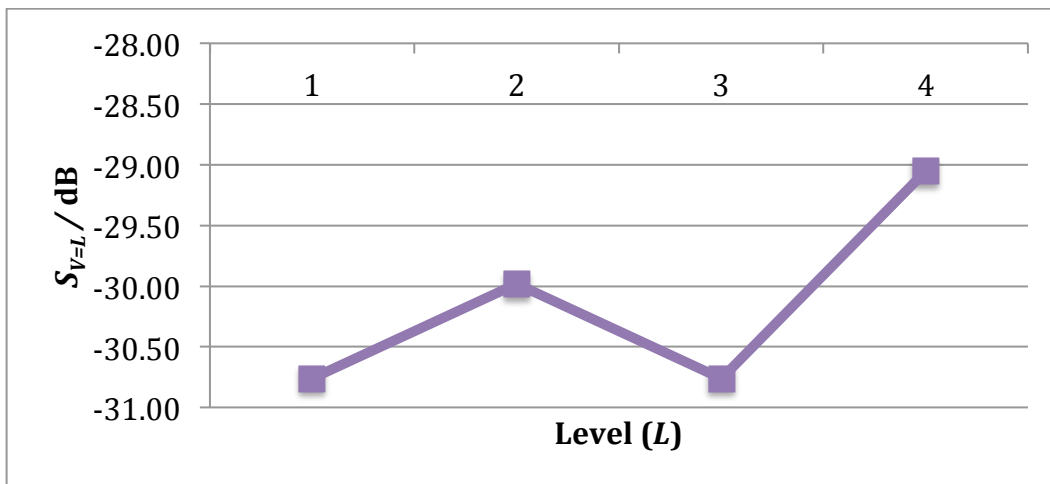
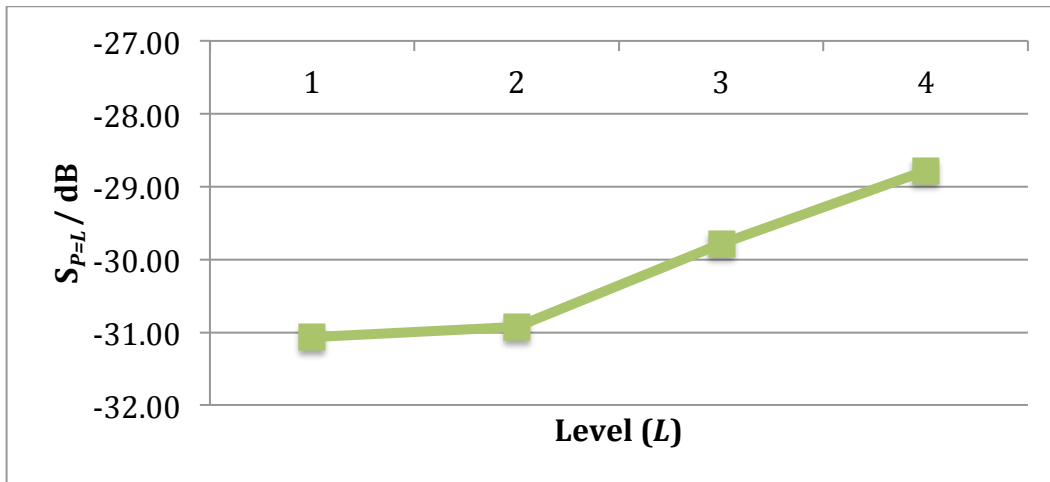


Figure 33: Plots of level against average signal to noise ratio for each level of each of the parameters: pressure (top), voltage (centre) and time (bottom).

From the plots given above, Taguchi optimization revealed the following levels to give the lowest CAs on average (Table 10):

Table 10: Optimum values derived from Taguchi optimization for the scrutinized variables.

Parameter	Optimum Level	Optimum Value
Pressure	4	0.1 Torr
Voltage	4	1.16 kV
Time	4	4 s

When another H-terminated sample was oxidized in the O₂ plasma reactor under the optimal conditions as detailed above, the mean CA was found to be $40.8 \pm 0.45^\circ$.

5.6. XPS

The first thing we obtain from the survey scan is a simple quantitative picture of the relative oxygen and carbon abundances, as provided from integration of each peak located at the typical binding energies for C 1s and O 1s core electrons (Table 11).

Table 11: Relative oxygen and carbon abundances of the five samples submitted for XPS analysis. The percentages provided are for the first few atomic layers concordant with the information depth of the Al K α X-ray photons.

Sample	Surface carbon abundance / %	Surface oxygen abundance / %
Control	95.49	4.51
Taguchi Optimum	86.58	13.42
4s O-termination	90.44	9.56
5s O-termination	83.74	16.26
10s O-termination	83.85	16.15

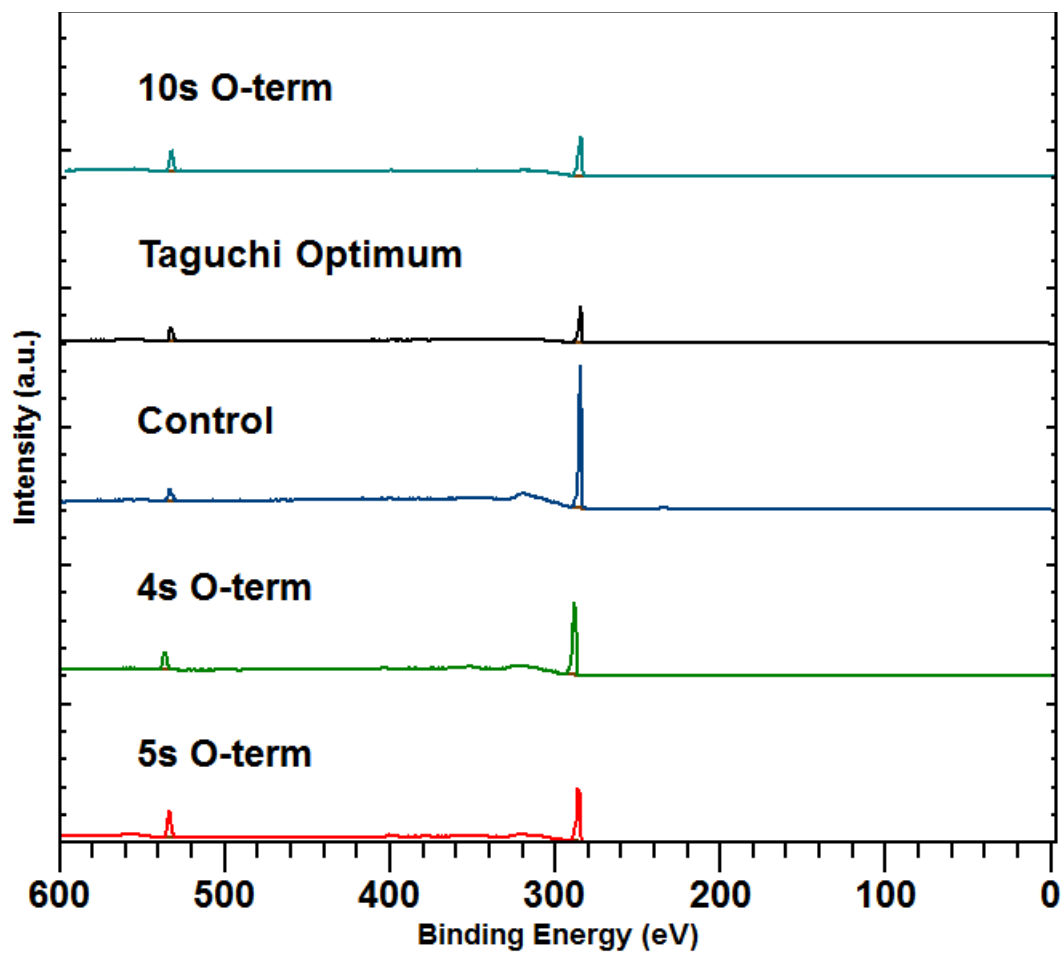


Figure 34: Overlaid survey scans for the five samples submitted for XPS analysis. The C1s and O1s peaks are centred on 285 and 532 eV, respectively.

The exact location of each peak maximum varies slightly from sample to sample (Fig. 34), as summarized below (Table 12).

Table 12: Exact binding energies for the C1s and O1s peaks obtained from the survey scans for all XPS analysed samples.

Sample	C1s BE / eV	O1s BE / eV
Control	284.8	533.3
Taguchi Optimum	284.8	532.8
4s O-termination	288.5	536.5
5s O-termination	286.0	533.5
10s O-termination	284.5	532.5

Upon peak fitting using CasaXPS, the chemically shifted components of each core peak are revealed, and can be identified based on previous experimentation. The binding energies for bulk diamond C-C bonds, C-O-C bridging ethers, C-OH alcohol groups, C=O carbonyl groups⁶² and graphitic C=C double bonds⁵⁶ are all known and so can justly be assigned. The values for each, in the solid state, are as shown in the table below. As aforementioned, it is perhaps better practice to use the difference in binding energy, Δ BE, to identify chemical shift. Hence also in the table below (Table 13) are the chemical shifts relative to the peak for the bulk C-C BE.

Table 13: Typical binding energy ranges for various functional groups present within the C1s core electron peak of an XPS spectrum.

Functional group	Binding energy / eV	Δ BE / eV
C=C	284.0	- 0.8 – 1.0
C-C or C-H	284.8 – 285.0	-
C-O-C or C-O-H	286.4 – 286.8	+ 1.4 – 2.0
C=O	287.9 – 288.0	+ 2.9 – 3.2

Thus all components within the C1s regions were identified, as displayed below (Fig. 35):

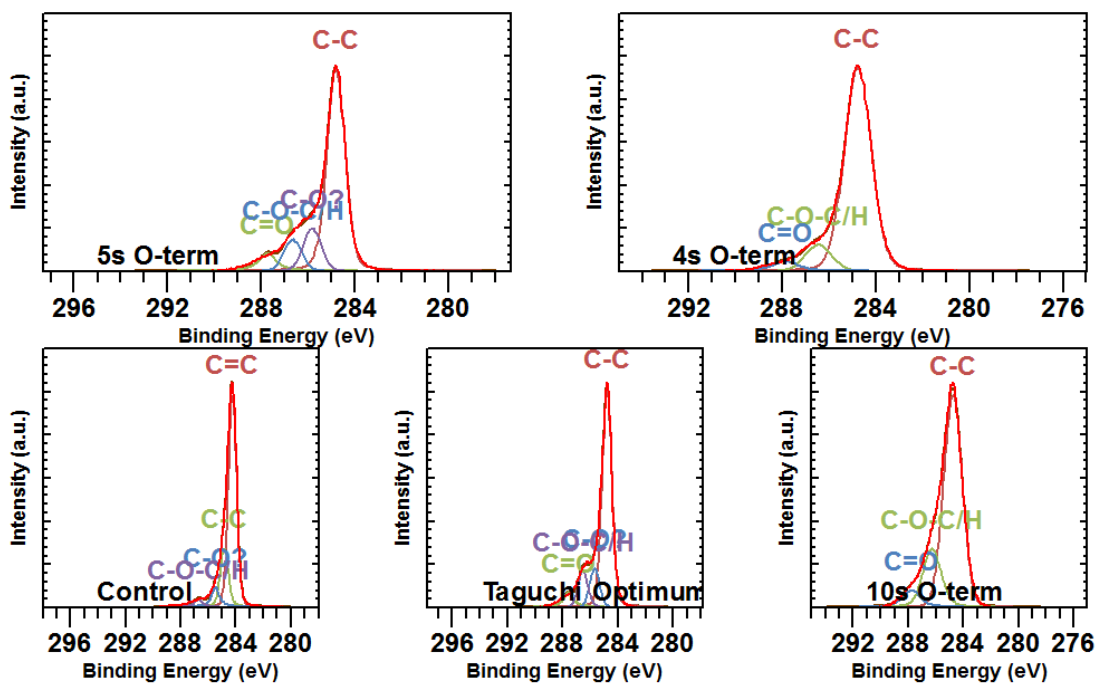


Figure 35: Fully assigned components of the C1s peaks. Note the discontinuity in colour of labels across different photoelectron spectra.

The photoelectron spectra of the 5 s O-terminated sample, the 0 s O-terminated sample (labelled Control) and the sample oxidized according to the optimal values according to the Taguchi method (labelled Taguchi Optimum) all contain an additional peak labelled “C-O?” within the energy range 285.5 – 285.8 eV ($\Delta BE +0.5 - 1.0$ eV). This peak had also been identified by O’Donnell *et al.* in similar work on diamond surfaces⁶³, yet remains to be fully characterized. Both peaks, labelled C-O-C/H and C-O?, are likely to correspond to bridging ethers and ketones whilst the peak labelled C=O corresponds to higher oxidation state anhydride or carboxylic groups^{64,65}.

The relative percentage abundances of each of the bonding modes can be extracted from peak fitting, again by integrating the area of each peak corresponding to each chemically shifted component (Table 14).

Table 14: Percentage abundance of each bonding mode detected by XPS by peak fitting within the C1s peak.

Sample	C=C / %	C-C or C-H / %	C-O? / %	C-O-C or C-O-H / %	C=O / %
Control	67.47	20.30	8.83	3.41	-
Taguchi Optimum	-	70.75	11.73	11.11	6.41
4s O-termination	-	84.55	-	10.34	5.11
5s O-termination	-	68.73	13.5	9.98	7.79
10s O-termination	-	71.93	-	21.14	6.94

Although the O1s peaks were identified and peak fitted for each of the 5 analysed samples, due to the lack of information on the chemical shifts of O1s components it appeared too difficult and unreliable to reap any information from them.

6. Discussion

6.1. SEM

The SEM micrographs confirmed, in a purely qualitative manner, that there was little to no topographical change upon surface oxidation with the O₂ plasma reactor. Unwanted surface reconstruction can be a consequence of other, more aggressive oxidation techniques and can be detrimental to diamond quality. Hence the relative softness of O₂ plasma oxidation is highly advantageous in safeguarding the desirable properties of diamond films.

The growth rate of 0.35 μm h⁻¹ was slightly lower than the expected value of 0.40 μm h⁻¹ previously achieved using the same reactor under the same operating conditions. The slower growth rate may have been a consequence of the lower than expected voltage passing through the filament, potentially leading to lower filament temperature and therefore diminishing gas activation. Yet the samples were sufficiently thick for our analytical purposes.

6.2. Laser Raman Spectroscopy

The data suggests that there was a certain degree of sp² character present in the CVD grown diamond samples, deduced from the fact that the FWHM has increased compared to that of the single crystal (100) samples. Although the standard deviation for FWHM is in fact smaller than that for the single crystal samples, so we can ascertain that there is a good consistency across samples. Similar can be said for the peak position which has moved to a slightly lower value for CVD grown samples, again indicating sp² presence, smaller crystallite size⁶⁶ or more simply, lesser diamond quality.

Knowing that the samples grown in the HFCVD reactor are polycrystalline, we expect peak broadening from the presence of different growth facets. Hence the larger FWHM value is not only permitted but also necessary in polycrystalline diamond. Overall the diamond quality was considered to be acceptable and sufficiently replicable for further investigation.

6.3. Preliminary investigation

The purpose of the preliminary investigation was to explore the efficacy, reliability and suitability of CA measurements as a means of determining the degree of oxidation of H-terminated diamond surfaces with the O₂ plasma reactor. Furthermore, the results were used to advise methodology and minimise error in subsequent experimentation. An important finding was the need to wait for droplet stabilization, as recommended by Berg⁶⁷.

A four second stabilisation time was allowed for each water droplet, as determined from viewing how long it takes for droplet CA to stabilize after deposition (Fig. 36). The time of droplet placement, t_0 , can be accurately determined using the ADVANCE program. The graph below shows that the CA doesn't plateau within the time-scale displayed, as complete stability is very unlikely to happen due to evaporation *etc.*, so the time for stabilisation of 4 seconds was selected as the point where the steepness of the curve tended to drop significantly across all observed samples. In setting a precise stabilisation time an extra variable was removed from wettability measurements.

Gribanovna²³ found CAs for hydrogen terminated surfaces to lie within the range of 70-75°. We did not find the same CA, but the authors of the paper didn't state

whether droplet stabilization was allowed, so it is feasible that they allowed for a longer stabilization time.

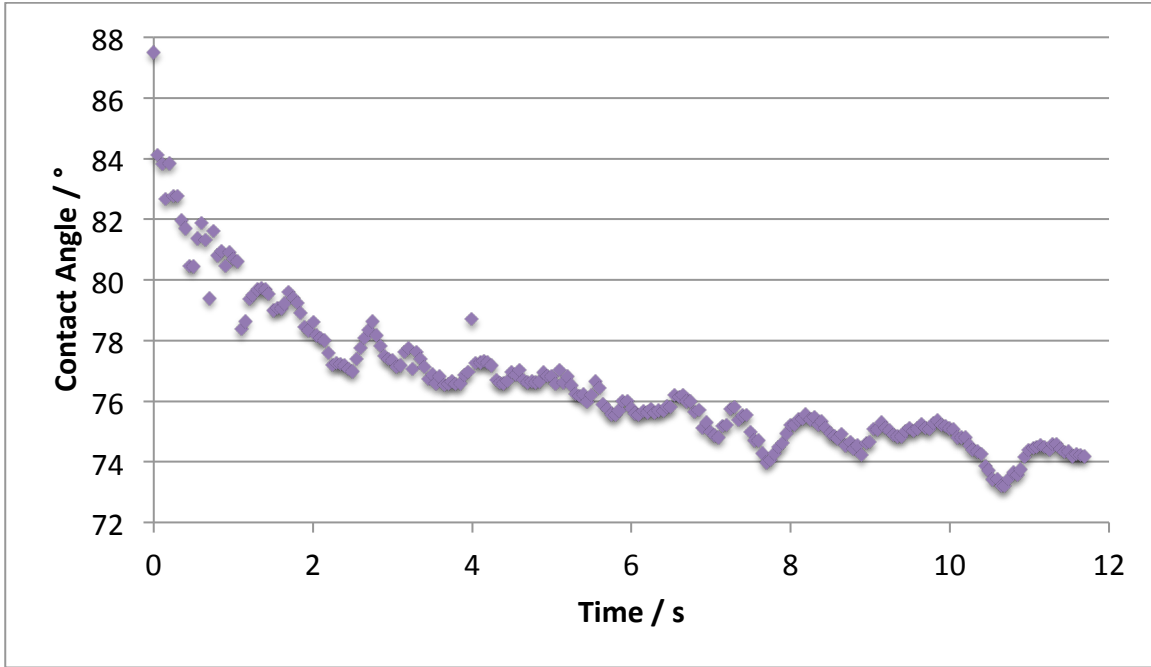


Figure 36: Graph demonstrating the diminution of the CA with time as the droplet spreads, for a droplet of water on a hydrogen-terminated diamond surface.

An issue with the initial wettability measurements is the variability, which although sometimes low ($< 0.05^\circ$), also yielded great errors ($\sim 6^\circ$), which were not within the range of $\pm 1 - 2^\circ$ observed by others^{22,23}. This variation most likely stems from heterogeneity or roughness of the diamond surface, again due to the nature of the multifaceted polycrystalline surface. Although the surface could have been smoothed, this would have contradicted the purpose of the experimentation, which was to justify the use of wettability analysis on as-grown CVD diamond surfaces.

The initial wettability measurements gave a local minimum of CA for 7 s of exposure to O₂ plasma, but if we examine the time-averaged CA against oxidized diamond surface curve (Fig. 30), whilst paying attention to the error bars we see that the minimum value for these particular conditions could give a minimum value anywhere between 5 and 8 s. Degradation and variation of CAs over time is unprecedented when we consider the significant energy input required to alter the diamond surface. Ageing of diamond samples is highly unlikely, thus ruling out surface changes, the variation must be within the wettability measurements themselves.

A whole host of reasons could be responsible for this variation: one factor could be the cleaning regime, which may be leaving solvent molecules physisorbed in microcracks on the surface²⁵. Equally, as samples weren't stored and transferred under vacuum, nor were measurements taken under vacuum, vapour molecules may have condensed on the surface. Both these factors are affected by ambient temperature as well as humidity, both of which were inconsistent and uncontrollable outside of vacuum conditions.

Furthermore, the decision was taken to measure CAs from different positions on the diamond surface in order to prevent physisorbed water molecules from contributing to repeat measurements. So whilst this method was designed to avoid skewing CAs, it may have contributed to the variation in measurement due to the heterogeneous nature of the surface. Seeing as there was such variation in both H-terminated and O-terminated diamond sample measurements from the same sample, it's difficult to determine whether this was a result of non-homogeneous hydrogen-termination and therefore discontinuous diamond growth or whether it's a result of the action of the O₂ plasma on the hydrogen-terminated diamond surface, or both.

The ADVANCE program in fact measures the left hand and right hand CA, from the perspective of the camera, made between the solid and liquid phase. The mean CA is also given and this is the one that has been used throughout this study. Droplet asymmetry was however frequently an issue and would again indicate incongruities even across such a small observed area. If we assume the droplet to be perfectly hemispherical with a volume of 2 μL , then using a simple 'back of envelope' calculation, the area of contact of a perfect hemisphere is calculated as $\sim 3 \text{ mm}^2$. This seemingly small exposed surface area however corresponds to on average 4.8×10^{13} carbon atoms exposed for an atomically smooth $\langle 100 \rangle$ Miller plane, and hence 9.6×10^{13} H-terminations, assuming 2 H-terminations per exposed carbon in a clean $\langle 100 \rangle$ Miller plane scission. These simple *a priori* calculations of course ignore the roughness and other Miller planes present on the CVD diamond surface, so in reality the figure would be much larger than this.

Finally, we must be aware of the human error present for the exposure time of the hydrogen-terminated surface to the O_2 plasma in the reactor. To run the voltage through the pure oxygen environment required manually engaging the power source at the same time as manually initiating a stopwatch. Thus for shorter time intervals the human error is more significant. Human reaction time is typically 0.25 s hence for 3 s of oxygen termination, this presents a significant error of $\pm 8.3 \%$ compared to just $\pm 2.5 \%$ for the 10 s oxygen termination. If the system were to be automated more accurate exposure times would be achieved.

6.4. SFE calculations

Despite the variability in CA as found in the preliminary work, the polar components of SFE agreed well with the measurements, as shown in the plot below (Fig. 37).

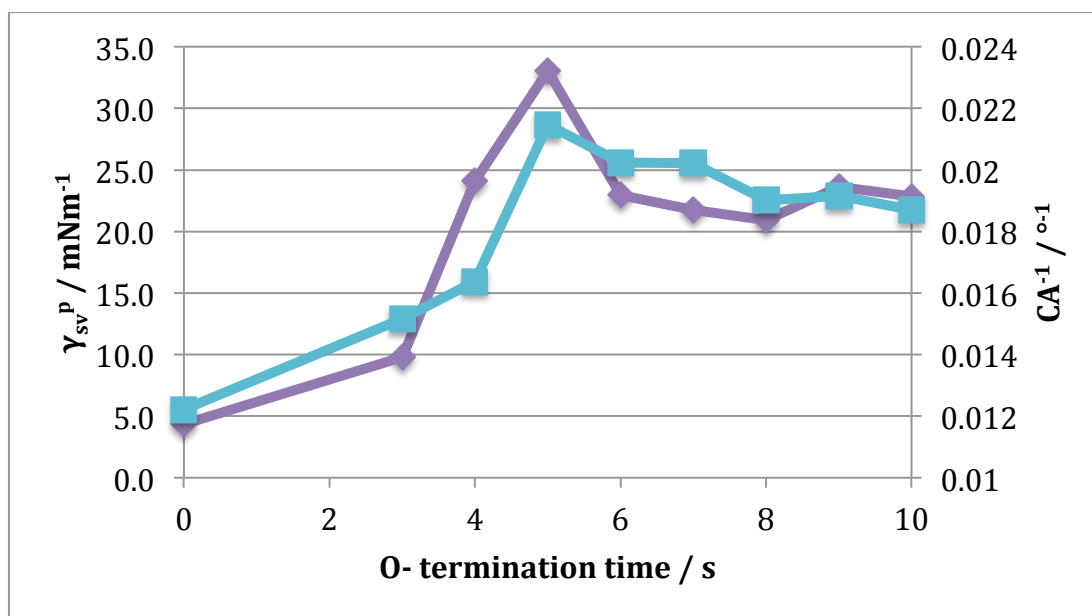


Figure 37: Plot comparing the polar component of the SFE and the inverse of the time-averaged CA measurement against the O-termination time. The data in purple correspond to the SFE values along with the left-hand axis, and the data in blue to the inverse CA measurements and the right-hand axis.

In the above plot, the CA measurements have been inverted so as to better demonstrate the comparable trends. We remark that the sample with the largest polar SFE component therefore also has the smallest CA, after five seconds of oxygen plasma exposure. The agreement is to be expected on the assumption that the polarity of the surface corresponds directly to the oxygen-containing moieties present on the oxidized diamond surfaces. So although the plots aren't equivalent, a strong correlation between the two is observed.

Of course we must remark that the largest polar component is for the 5 s O-terminated sample and from Figure 32 that the disperse component is fairly consistent from the 4 s O-terminated sample onwards. If the disperse portion defines the proportion of C atoms with remaining H-terminations, then this data suggests that from four seconds onwards all the possible H atoms are removed, and in fact the variation in polarity and hence smaller CA is merely a result of the kinds of O-terminations present on the oxidized diamond surface. Although this is in disagreement with the XPS findings as discussed later.

Changing the liquid phase, as is necessary for SFE calculation, leaves CA measurements susceptible to the same issues as using water alone as a liquid phase. The methodology used here was slightly different to that used in the preliminary work, as here each liquid phase droplet was placed in the same position on the sample, perhaps rendering it less liable to variation through surface heterogeneity. Nonetheless, the R^2 value for all SFE graphs of the type in Figure 31, using the Owens-Wendt method, were within the range 0.94694 – 0.99997, showing a strong correlation. These strong correlations are however for a linear plot containing just three points, so more liquid phases could weaken it.

6.5. Taguchi Optimization

In order to seek the optimum conditions for oxidation of a H-terminated diamond sample, using the O₂ plasma reactor, I performed a Taguchi optimization. The Taguchi Method, which was originally devised as a statistical approach to business amelioration, but applied to a reactor, it allows determination of optimum operating

conditions with much fewer test runs than would be needed for a full factorial analysis.

To start off the Taguchi Method we first identify key variables affecting product quality. Possible variables of the plasma reactor, which are liable to remark noticeable change on the oxidation of the diamond surface, were:

- 1) Gas composition
- 2) Pressure
- 3) Voltage
- 4) Time
- 5) Total mass flow

The gas composition could have been altered to incorporate gaseous argon in to the reaction chamber, however this was deemed unnecessary to do so. The reasons for which are that firstly, the breakdown voltage required to initiate and sustain stable oxygen plasma was satisfactorily low without the addition of Ar. Photodissociation of O_2 to two ground state $O(^3P)$ atoms requires an input of 5.1 eV⁶⁸, which is much smaller than the 15.76 eV required⁶⁹ for Ar ionisation to Ar^+ . Thus the incorporation of Ar in to the reaction chamber wouldn't affect η , the secondary ionisation constant, as it does upon addition of Ar to Ne gas where the energy of metastable states is greater than that for the ionisation of Ar^[52]. Hence the breakdown voltage will not reduce upon Ar addition *via* the inverse relationship for $V_b \propto 1/\eta$ as shown in full:

$$V_b = (-\ln y)/\eta \quad (18)$$

Secondly, the rotary pump can easily withstand such small amounts of O_2 , thus not presenting a safety hazard through rapid oil consumption. Thirdly, by the same

argument as for the first point, the quantity of reactive photo-excited O₂ species is not enhanced on Ar addition.

The total mass flow was again not deemed to adversely affect surface oxidation. The flow rate of 10 sccm for O₂ was the maximum possible for the particular MFC used, and due to the self-sustaining nature of the arc-discharge, the flow rate in to the chamber was considered sufficient to replace any O₂ used up in surface oxidation. It was assumed then that lowering the total mass flow could then only have a possible negative impact on the self-sustainability of the plasma. Hence total mass flow and gas composition were discounted from Taguchi optimization and were consequently set as constants, whilst pressure, voltage and time were varied.

Preliminary work assisted in selecting reasonable values for time, voltage and pressure while ensuring continuous plasma within the operating limits of the reactor. Once decided, the orthogonal array was selected depending on the number of levels desired for each variable. Due to the amount of time needed to grow a large number of CVD diamond samples, the orthogonal array chosen gave 16 permutations of reaction conditions to run with the L₁₆ matrix selected, rather than the 64 that would be needed for full factorial analysis.

Next a key observable had to be selected to measure the successful oxidation of the diamond surface, which ascertains to heightened product quality, which was surface wetting. For the purposes of the Taguchi analysis this observable alone was deemed sufficient to quantify the surface oxidation. Yagi *et al.*³² used an RF plasma at 0.15 Torr which gave no change of surface morphology with exposure to plasma from 1 – 60 s, so etching and surface morphology changes were again not used as observables in Taguchi optimization.

When analysing the results, it is interesting to remark that for some of the samples, of the 4 CA measurements taken, it appears that two of the CAs are close in value and significantly different than the other two which are similarly approximate to one another. As the 4 measurements were taken adjacent to the 4 corners this may suggest an oxidation gradient across samples, thus insinuating inconsistent O₂ plasma. This phenomenon of inconsistent oxidation is further supported when we regard the errors, which in one case (Run 11) was > 13°. The mean standard deviation for the Taguchi analysis was found to be ± 4.2°, which is significantly larger than the mean standard deviation across the non-time averaged preliminary results found to be ± 1.82°.

The oxidized diamond sample as modified in accordance with the results of the Taguchi optimization was found to have a mean CA of 40.8 ± 0.5°, using water as a liquid phase, which was no less than the CA for the final run (Run 16) of the Taguchi analysis with an angle of 38.9 ± 0.7°. The CA was however smaller than that of all other oxidized surfaces in the Taguchi analysis and of those carried out in the preliminary work. Both the 'Taguchi Optimum' sample and the sample in run 16 were modified in the O₂ plasma reactor at a pressure of 0.1 Torr (Level 4) and at a voltage of 1.16 kV (Level 4). The only difference is that the 'Taguchi Optimum' was exposed to the plasma for four seconds (Level 4) whilst the sample from run 16 was exposed for ten seconds (Level 1). Therefore what becomes apparent is that the low voltage and pressure used to modify both these samples is necessary for low CA measurements, yet the optimum duration of plasma exposure is yet to be determined. Additionally, the S/N ratios for the third and fourth level of the time variable are very similar (Table 9/Fig. 33), again expressing a lack of preference for particular plasma exposure duration.

For all voltages explored from 0.2 - 2.1 kV the plasma would glow and be self-sustaining whilst maintaining a current within the mA range. However at lower voltages, the plasma would glow more dimly and would glow more brightly at higher voltages. Also upon changing the pressure within the stable plasma region, the plasma is highly disperse at low pressures and on heading towards the 2 Torr limit for plasma stability, the plasma becomes more focussed between the two flat plate electrodes. The Taguchi findings evince the preference for this dim, disperse, less energetic and less concentrated plasma in order to gives smaller CAs, but unfortunately without a deep understanding of plasma physics I am unable to offer detailed reasons as to why. Yet I postulate that highly localised plasma reduces active ion mobility, and higher voltages provoke an increase in excited state O₂ without increasing ionic activated oxygen molecules, therefore restricting oxidation.

6.6. XPS

XPS analysis, being both temporally and financially costly, was carried out on just a few select samples, despite it providing the most complete picture of surface bonding and relative abundances. Initially we can perform a simple comparison of CA measurement with percentage atomic oxygen abundance as obtained from the survey scan, to clarify the relationship between them, as shown in the table below (Table 15):

Table 15: Percentage atomic oxygen obtained from peak integration of the XPS survey scan for modified diamond surfaces, with comparison to their CA measurements, using water as the liquid phase.

Sample	Survey atomic oxygen / %	CA / °
Control	4.51	83.0
4s O-term	9.56	61.1
5s O-term	16.26	47.3
10s O-term	16.15	53.6
Taguchi Optimum	13.42	40.8

The above table shows a fairly good correlation between CA and percentage oxygen, apart from the outlier of the Taguchi Optimum, which gives the lowest CA of the samples considered in XPS analysis, but not the largest surface oxygen coverage. This phenomenon could only be explained by the reasoning that the Taguchi Optimum sample harbours more polar oxidized moieties, assuming that both the angles and XPS data are correct. Also this is perhaps easier to visualise graphically, as redisplayed below (Fig. 38). As before, inverse CA measurements have been used for clarity, seeing as the smallest CA should correspond to the highest oxygen percentage.

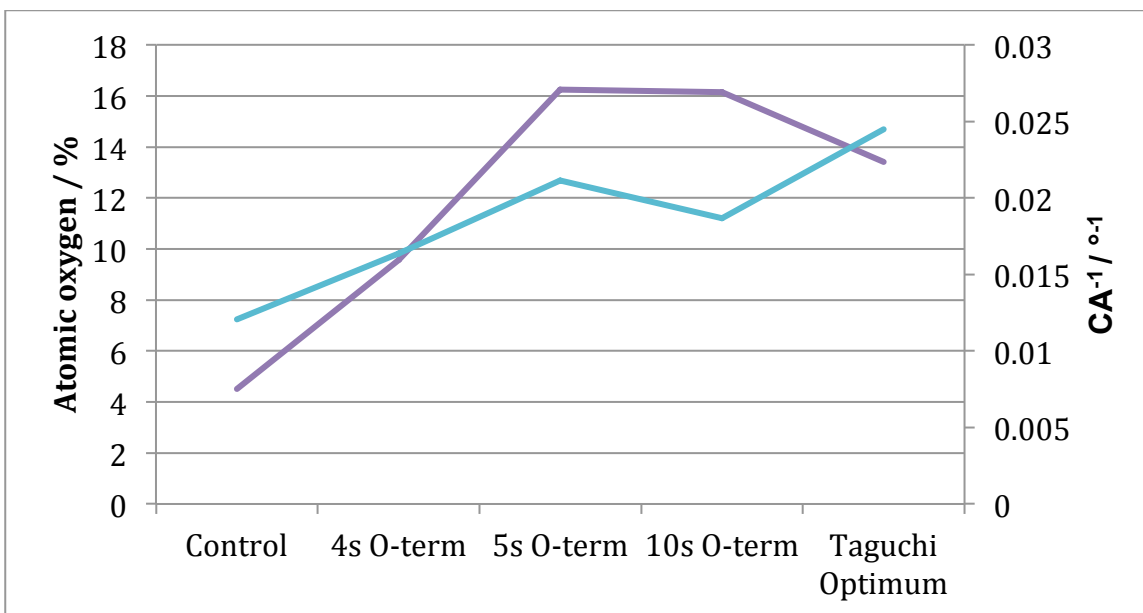


Figure 38: Plot of percentage atomic oxygen as obtained from the survey scan (purple) on XPS analysed samples, overlaid with inverse CA measurements (blue).

Further scrutinizing Figure 38 reveals the correlation between CA and percentage atomic oxygen is weak, as although the linear plots have similar shapes (bar the point for the Taguchi Optimum), the gradients of the adjoining lines between measurements are unequal. Although the maximum surface coverage of ~16% atomic oxygen is in good agreement with the findings of Yang and Wang^{62,65}.

Referring to Table 12, the phenomenon of ‘charging’ is the reason that many of the peak centres were shifted to slightly higher binding energies. The diamond samples were electrically insulating, undoped samples, so when X-ray photons strike the surface, causing emission of electrons, positive charges can form and accumulate at the surface, shifting peaks to higher binding energies. This occurrence doesn’t affect the quality of the information provided as we observed ΔBE to identify chemically shifted regions, rather than absolute values of BE.

Next I must address the large graphitic sp^2 carbon peak at ~ 284.0 eV in the C1s scan (Table 14/Fig. 35), for the control H-terminated sample. Admittedly, not enough care and attention was taken in the selection of the control sample, as it was assumed to be as good quality diamond as all other samples it was somewhat chosen at random. It would appear however that this was not the case. It was most likely that this sample suffered difficulties during CVD diamond growth itself, seeing as the sample will not have been exposed to high temperatures likely to affect such surface reconstruction prior to XPS analysis. Also the presence of an oxygen peak is not entirely unusual⁷⁰, yet the large percentage atomic oxygen of $\sim 4.5\%$ is abnormal. Torrenco *et al.*⁷⁰, found oxygen abundance on the order of 1% for diamond grown under similar operating conditions. This significant oxygen percentage is likely a consequence of exposing the CVD grown diamond sample to air after an insufficient amount of cooling time within the reactor. Although as I am unable to confirm this was the case, this value cannot be ignored. It is however reassuring that no other C1s peaks gave a similar sp^2 carbon response, perhaps indicating an anomalous H-terminated sample.

For greater analysis of the C1s peak and its substituents, we must comprehend to what depth the sample was analysed, known as the information depth (ID). The Al K_{α} 1486.7 eV monochromatic photoelectrons provokes emission of photoelectrons with a kinetic energy of 1202 eV, once the BE of C1s has been subtracted. The attenuation length (AL)⁷¹ for a photoelectron with this KE is 3.4 nm, defined as the average distance an electron travels between inelastic interactions, and is obtained from a 'universal curve' for organic materials, as defined by Seah and Dench⁷². This AL is similar to the inelastic mean free path (IMFP) in that it is a measure of surface sensitivity⁷³ in electron spectroscopy, and both can be used to determine the ID for a sample. The difference being that the ID accounting for 99.3% of the observed signal is equal to five times the escape depth (ED), whilst the ID accounting for 95% of the

observed signal is equal to three times the IMFP. Before we arrive at the ID we must define another term, the ED, which is a direct measure of surface sensitivity in units of length, just like the ID, IMFP and AL. ED however accounts for the take off angle, θ , defined as the angle at which the detector is placed, relative to the normal of the sample surface. ED is defined by the following equation:

$$ED = AL \cos \theta \quad (19)$$

The take off angle used in our experimentation was 84° , so from an AL of 4.0 nm, the ED becomes 0.418 nm, finally giving an ID of 2.09 nm for the C1s peak. Although similarly we could arrive at an ID of 1.38 nm *via* multiplication of the IMFP value of 4.4 nm for the C1s peak, as given by Ashley⁷⁴. Using the ID as derived through ED determination, and multiplying by the total percentage oxygen abundance (31.27%) from the summation of oxygen containing chemically shifted regions of the 5 s O-terminated sample C1s peak (Table 14), gives an oxidized surface layer thickness of ~ 0.7 nm, equal to that as found by Yang *et al.*⁶².

Continuing with the idea that the Taguchi Optimum sample must harbour more polar oxidized surface functional groups; we notice that both the 5 s O-terminated sample and the Taguchi Optimum harbour the component labelled "C-O?" with a BE of 285.5 – 285.8 eV (Fig. 35). These two samples also give the lowest CAs, so perhaps this functional group is highly polar. To investigate further, we again employed a graphical interpretation to seek confirmation of the theory. The plot below (Fig. 39) depicts the inversed CA alongside the percentage atomic oxygen for the region labelled "C-O?" in the C1s peak. A second overlaid data set is shown which plots the sum of the C-O? peak and the peak with a BE of 287.9 – 288.0 eV, labelled C=O. As aforementioned, the peaks corresponding to these specific binding energies are likely to correspond to bridging ethers and ketones (C-O?) whilst the peak labelled C=O corresponds to higher oxidation state anhydride or carboxylic

groups^{63,64,65}, and is further supported by the findings of Laikhtman *et al.*, using high resolution electron energy loss spectroscopy (HREELS)⁷⁵.

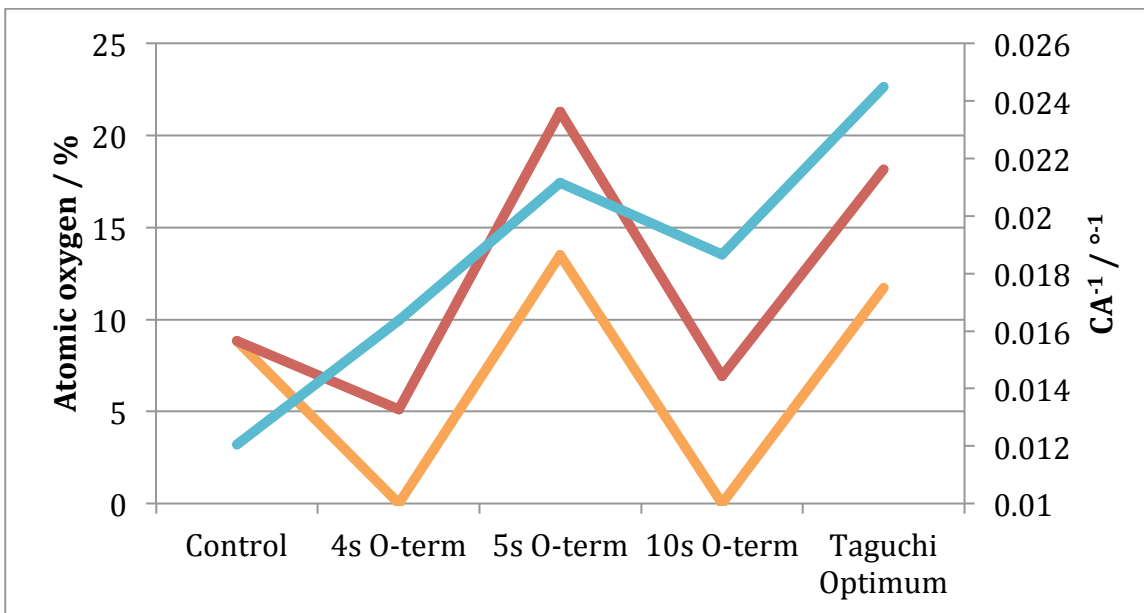


Figure 39: Inverse CA (blue) overlaid with the percentage atomic oxygen as obtained from the C1s peak for the component at 285.5 – 285.8 eV alone (orange), and that same component combined with the component at 287.9 – 288.0 eV (red).

The above curve shows a similar situation to Figure 38, where the CA could be assimilated to follow the percentage atomic oxygen plots, where the peak summation of the polar moieties purveys a better fit. Although there appears to be a significant outlying data point, found in the control sample. Again, we must be cautious in rejecting data as invalid, but perhaps it was the poor selection of a control sample that accounts for this anomaly. Of course, such a claim warrants further investigation with a 'better', more representative control sample for H-terminated CVD-grown diamond. Furthermore, the summation of these polar moiety concentrations still gives a larger percentage for the 5 s O-terminated

sample than the Taguchi Optimum, hence still not accounting for the Taguchi Optimum sample's smaller CA.

The reason for all this discontinuity could lie in the fact that the XPS analysis was carried out in the centre of the samples in a small area, whilst the CA measurements were taken from the entirety of each sample. Therefore XPS analyses should have been carried out over the whole sample, as with CA measurements, or alternatively CA measurements taken from a single point, as in XPS. In other words, the Taguchi Optimum percentage atomic oxygen may not be representative of the whole sample. The disparity between these atomic percentages and CAs stresses the necessity of repeat XPS analyses, as done by Yang *et al.*^[62], but unfortunately neither time nor money made allowed this.

7. Conclusions and Further Work

The purpose of this study was two-fold: to query the efficacy of wettability measurements in quantifying surface oxidation of diamond surfaces and to optimize the new O₂ plasma system for said oxidation. Wettability investigation was carried out on as-grown polycrystalline CVD diamond samples, which eventually presented numerous problems. Heterogeneity stemming from the multifaceted diamond surfaces meant that CA measurements presented much larger errors than were reasonably permitted. For this reason, similar investigation should be carried out with single-diamond samples of the most prevalent diamond growth planes ((100) and (111)) in polycrystalline diamond. Similar work has been carried out by Wang *et al.*⁶⁵ where the oxidation was undertaken using a wet chemical method, which should be replaced by the O₂ plasma reactor in future work. A thorough study of this kind would reveal whether CA measurements are indeed a viable method for quantifying this type of oxidation, with follow-up work using XPS.

The lack of homogeneity across an oxidized diamond sample could have been due to the fluid dynamics or method of action of the plasma itself. The mechanism of oxidation of H-terminated diamond surfaces by oxygen plasma has not been explored here, and would be of great interest to truly understand the process of oxidation. Mark Kelly PhD, of the Bristol Diamond Group, carried out similar work seeking to understand plasma operation in CVD techniques in 2014 using computer modelling. Molecular Mechanical (MM) and Quantum Mechanical (QM) computational methods were used in combination (QM/MM) with cavity ring down spectroscopy (CRDS) to identify active species in CVD growth using CH₄/CO₂/H₂ plasma. As such, a complete investigation in to oxygen plasma surface modification of an H-terminated diamond surface should be explored, also in combination with optical emission spectroscopy (OES)⁷⁶, as a non-invasive plasma probing technique.

It was found that the oxygen plasma might have been oxidizing the diamond surface to different degrees across the sample surface. In order to determine whether this is the case, transverse OES spatial profiling could be used just above the diamond surface to verify a possible concentration gradient of active oxygen species across the surface. Equally, one could seek to identify whether species produced after oxidation are re-depositing hydrogen or are spatially restricted post-oxidation.

Percentage atomic oxygen abundances, as found through XPS analysis, were found not to correlate exactly with CA measurements. It was deduced that this might have been avoided if wettability measurements and XPS analyses were performed on the same precise location of each sample, whilst still working with polycrystalline diamond samples. The surface area exposed to the liquid phase of a wettability

measurement could be estimated from the droplet CA and volume. Then specifically this known surface area could be subjected to further analysis by XPS.

There was a common component of the C1s peak that was identified in the control, 5 s O-terminated sample and the Taguchi Optimum sample, labelled C-0?. This peak had a BE of 285.5 – 285.8 eV, and has yet to be assigned to a specific functional group. The functional group is expected to be highly polar and essential to providing low CA measurements. Experimentation like that of Yang *et al.*⁶², where surface functional groups were derivatized with fluorine containing groups, could allow the moiety to be identified. The derivatization was followed with further XPS analysis, where the fluorine containing groups caused much-exaggerated chemical shift, eventually permitting group identification based on known reactivity of functional groups.

All research carried out in this project could have been further enhanced by the use of Tunnelling Atomic Force Microscopy (TUNA), as carried out by Dr Robert Harniman at the University of Bristol. TUNA analysis permits surface conductivity measurements on the nanometre scale, and hence presents another method of precisely determining surface oxygen coverage, as well as enabling surface functional group identification. Unfortunately Dr Harniman's busy schedule meant that this level of analysis was not carried out within the timeframe of my project, yet the same samples as analysed by XPS have been submitted for later analysis.

Taguchi optimization was successful in producing diamond surfaces with low CAs, although XPS analysis didn't reinforce that these low CAs correlate to greater oxygen surface coverage. In addition, the sample that gave the lowest CA within the orthogonal array did not correspond to the sample oxidized in accordance with the

results of the Taguchi analysis. Both samples were however oxidized in the reactor at the lowest pressure level (0.1 Torr) and lowest voltage level (1.16 kV). It would therefore appear that the optimum duration of plasma exposure is yet to be determined. An investigation similar to that carried out in the preliminary investigation, where the time of plasma exposure was varied solely whilst the voltage and pressure were kept constant, could be repeated under the new conditions of low pressure and voltage as found in the Taguchi analysis. Further to this, the full ranges of voltages necessary to give continuous arc discharge plasma were not explored in the Taguchi optimization. Thus it is feasible that lower CAs and greater oxidation could be achieved using a lower voltage than that resultant from the analysis.

Finally, the polar component of the SFE was found to be in good agreement with the CA measurements, indicating that the more polar the surface, the lower the CA. Although the use of just three liquid phases in the Owens-Wendt method for SFE calculation is unreliable. The relationship must be confirmed by taking by complimentary wettability measurements using a greater variety of liquid phases with varying polar and dispersed components of SFE.

-
- ¹ R. Berman, in *Physical Properties of Diamond*, Oxford University Press, London (1965),
- ² P.W. May, *Phil. Trans. R. Soc. Lond. A*, 2000, **358**, 473
- ³ H. O. Pierson, in *Handbook of Carbon, Graphite, Diamond and Fullerenes*, Noyes Publications, Park Ridge, New Jersey (1993)
- ⁴ P.W. May, *Science*, 2008, **319**, 1490
- ⁵ F.P. Bundy, *Physica A*, 1989, **156**, 169
- ⁶ H. Lui and D. S. Dandy, in *Diamond Chemical Vapour Deposition: Nucleation and Early Growth Stages*, Noyes Publications, Park Ridge, New Jersey (1995)
- ⁷ J. M. Zazula, "On Graphite Transformation at High Temperature and Pressure Induced by Absorption of the LHC Beam", CERN-SL/BT(TA), Geneva (January 1997)
- ⁸ S. Matsumoto, Y. Sato, M. Kamo, and N. Setaka, *Jpn. J. Appl. Phys.*, 1982, **21**, L183
- ⁹ J. C. Angus and C. C. Hayman, *Science*, 1988, **241**, 913
- ¹⁰ X. Jiang and C. P. Klages, *Diam. Relat. Mater.*, 1993, **2**, 1112
- ¹¹ W. A. Yarbrough and R. Messier, *Science*, 1990, **247**, 688
- ¹² G. Kern, J. Hafner and G. Kresse, *Surf. Sci.*, 1996, **366**, 464
- ¹³ X. Luo, Z. Liu, B. Xu, D. Yu, Y. Tian, H. Wang and J. He, *J. Phys. Chem. C*, 2010, **114**, 17851
- ¹⁴ A. W. Adamson, in *Physical Chemistry of Surfaces*, Interscience, New York, 2nd Ed (1967), 253
- ¹⁵ J. J. Gilman, *J. Appl. Phys.*, 1960, **31**, 2208
- ¹⁶ T. Halicioglu, *Surf. Sci. Lett.*, 1991, **259**, L714
- ¹⁷ G. Kern, J. Hafner and G. Kresse, *Surf. Sci.*, 1996, **366**, 445
- ¹⁸ A. Scholze, W. G. Schmidt and F. Bechstedt, *Phys. Rev. B*, 1996, **53**, 13725
- ¹⁹ Y. Yu, C. Z. Gu, L. F. Xu and S. B. Zhang, *Phys. Rev. B*, 2004, **70**, 125423
- ²⁰ T. Ando, K. Yamamoto, M. Ishii, M. Kamo and Y. Sato, *J. Chem. Soc. Faraday Trans.*, 1993, **89**, 3635
- ²¹ <https://www.kruss.de/services/education-theory/glossary/static-contact-angle/>
- ²² L. Ostrovskaya, V. Perevertailo, V. Ralchenko, A. Dementjev and O. Loginova, *Diamond Relat. Mater.*, 2002, **11**, 845

-
- ²³ E. V. Gribanova, A. N. Zhukov, I. E. Antonyuk, C. Benndorf and E.N. Baskova, *Diamond Relat. Mater.*, 2000, **9**, 1
- ²⁴ F. M. Fowkes, in *Chemistry and Physics of Interfaces*, American Chemical Society, Washington, (1965), 1
- ²⁵ J. O. Hansen, R.G. Copperthwaite, T.E. Derry and J.M. Pratt, *J. Colloid. Interface Sci.*, 1989, **130**, 347
- ²⁶ R. N. Wenzel, *Ind. Eng. Chem.*, 1936, **28**, 988
- ²⁷ F. Klauser, S. Ghodbane, R. Boukherroub, S. Szunerits, D. Steinmüller-Nethl, E. Bertel, N. Memmel, *Diam. Relat. Mater.*, 2010, **19**, 474
- ²⁸ K. Sugata, M. Tachiki, T. Fukuda, H. Seo and H. Kwarada, *Jpn. J. Appl. Phys.*, 2002, **41**, 4983
- ²⁹ Y. Kaibara, K. Sugata, M. Tachiki, H. Umezawa and H. Kwarada, *Diam. Relat. Mater.*, 2003, **12**, 560
- ³⁰ R. Sappok and H.P. Boehm, *Carbon*, 1968, **6**, 573
- ³¹ S. Szunerits and R. Boukherroub, *J Solid State Electrochem*, 2008, **12**, 1205
- ³² I. Yagi, H. Notsu, T. Kondo, D. A. Tryk, and A. Fujishima, *Journal of Electroanalytical Chemistry*, 1999, **473**, 173
- ³³ H. Notsu, T. Fukazawa, T. Tatsuma, D.A. Tryk and A. Fujishima, *Electrochem Solid-State Lett* , 2001, **4**, H1
- ³⁴ E. Brillas and C. A. Martínez-Huitle, in *Synthetic Diamond Films: Preparation, Electrochemistry, Characterization, and Applications*, Wiley, New Jersey (2011)
- ³⁵ J. Wilks and Eileen Wilks, in *Properties and Applications of Diamonds*, Butterworth-Heinemann Ltd, Oxford (1991), 63-81
- ³⁶ D. J. Poferl, N. C. Gardner, J. C. Angus, *J. Appl. Phys.*, 1973, **44**, 1428
- ³⁷ D. A. Fraser, in *The Physics of semi-conductor devices*, Clarendon Press, Oxford (1977)
- ³⁸ P. Atkins, J. de Paula and R. Friedman, in *Physical Chemistry: Quanta, Matter, and Change*, Oxford University Press, Oxford, 2nd Ed (2014), 353-357
- ³⁹ M. Nesdaiek, *Semicond. Sci. Technol.*, 2005, **20**, R19

-
- ⁴⁰ H. M. Rosenberg, in *The solid state: an introduction to the physics of crystals for students of physics, materials science, and engineering*, Clarendon Press, Oxford (1975), Chapters 7-9
- ⁴¹ T. Maki, S. Shikama, M. Komori, Y. Sakaguchi, K. Sakuta and T. Kobayashi, *Jpn. J. Appl. Phys.*, 1992, **31**, L1446
- ⁴² Z. Zhang and J. T. Yates Jr., *Chem. Rev.*, 2012, **112**, 5520
- ⁴³ I. L. Krainsky and V. M. Asnin, *Appl. Phys. Lett.*, 1998, **72**, 2574
- ⁴⁴ J. van der Weide, Z. Zhang, P. K. Baumann, M. G. Wensell, J. Bernholc and R. J. Nemanich, *Phys. Rev. B*, 1994, **50**, 5803
- ⁴⁵ J. R. Smith, G. L. Bilbro and R. J. Nemanich, *Diam. Relat. Mater.*, 2006, **15**, 2082
- ⁴⁶ D. Takeuchi, S. -G. Ri, N. Tokuda and S. Yamasaki, *Diam. Relat. Mater.*, 2009, **18**, 206
- ⁴⁷ K. P. Loh, J. S. Foord, R. G. Egdell and R. B. Jackman, *Diam. Relat. Mater.*, 1997, **6**, 874
- ⁴⁸ M. W. Geiss, J. C. Twichell, J. Macaulay and K. Okano, *Appl. Phys. Lett.*, 1995, **67**, 1328
- ⁴⁹ S. Okoli, R. Haubner and B. Lux, *Journal de Physique IV Colloque*, 1991, **2**, C2-923
- ⁵⁰ L. E. Smart and E. A. Moore, in *Solid State Chemistry: An Introduction*, CRC Press, Boca Raton, 4th Ed (2012), 101-104
- ⁵¹ A. M. Howatson, in *An Introduction to Gas Discharges*, Pergamon Press, Oxford, 2nd Ed (1976), 1-5
- ⁵² F. M. Penning, in *Electrical Discharges in Gases*, Cleaver-Hume Press, London, 2nd Ed (1965)
- ⁵³ R. G. Buckley, T. D. Moustakas, L. Ye and J. Varon, *J. Appl. Phys.*, 1989, **66**, 3595
- ⁵⁴ J. Wagner, C. Wild, W. Müller-Sebert, and P. Koidl, *Appl. Phys. Lett.* , 1992, **61**, 1284
- ⁵⁵ D. Briggs, in *Handbook of X-ray and Ultraviolet Photoelectron Spectroscopy*, Heyden, London (1977)
- ⁵⁶ T. A. Carlson, in *Photoelectron and Auger Spectroscopy*, Plenum Press, New York (1975), 165 - 198
- ⁵⁷ V. Lockett, R. Sedev, C. Bassell and J. Ralston, *Phys. Chem. Chem. Phys.*, 2008, **10**, 1330
- ⁵⁸ A. Bendell, J. Disney and W.A. Pridmore, in *Taguchi Methods: Applications in World Industry*, IFS Publications, UK (1989), 1-11

-
- ⁵⁹ G. Taguchi, E. A. Elsayed and T. C. Hsiang, in *Quality Engineering in Production Systems*, McGraw-Hill Book Company, New York (1989)
- ⁶⁰ D. Briggs and M.P. Seah, in *Practical Surface Analysis*, John Wiley & Sons, Chichester, 2nd Ed (1990), 641
- ⁶¹ P. van der Heide, in *X-Ray Photoelectron Spectroscopy: An Introduction to Principles and Practices*, Wiley, New Jersey (2012), 135-138
- ⁶² M. Yang, M. J. Marino, V. J. Bojan, O. L. Eryilmaz, A. Erdemir and S. H. Kim, *Appl. Surf. Sci.*, 2011, **257**, 7633
- ⁶³ K. M. O'Donnell, M. T. Edmonds, J. Ristein, A. Tadich, L. Thomsen, Q. Wu, C. I. Pakes and L. Ley, *Adv. Funct. Mater.*, 2013, **23**, 5608
- ⁶⁴ K.P. Loh, X. N. Xie, Y. H. Lim, E. J. Teo, J. C. Zheng and T. Ando, *Surf. Sci.*, 2002, **505**, 93
- ⁶⁵ X. Wang, A. Rahim Ruslinda, Y. Ishiyama, Y. Ishii and H. Kawarada, *Diam. Relat. Mater.*, 2011, **20**, 1319
- ⁶⁶ M. Yoshikawa, G. Katagiri, H. Ishida, A. Ishitani, M. Ono and K. Matsumura, *Appl. Phys. Lett.*, 1989, **55**, 2608
- ⁶⁷ J. C. Berg, in *Wettability*, Marcel Dekker, Inc., New York (1993), 1-71
- ⁶⁸ T. G. Slinger and R. A. Copeland, *Chem. Rev.*, 2003, **103**, 4731
- ⁶⁹ D. R. Lide, in *CRC Handbook of Chemistry and Physics*, CRC Press, Boca Raton, 84th Ed (2003), Section 10
- ⁷⁰ S. Torrenco, R. Canteri, R. Dell'Anna, L. Minati, A. Pasquarelli and G. Speranza, *Appl. Surf. Sci.*, 2013, **276**, 101
- ⁷¹ N. Suzuki, K. Imura, S. Satoh, Y. Saito, T. Kato and A. Tanaka, *Surface and Interface Analysis*, 1997, **25**, 650
- ⁷² M. P. Seah and W. A. Dench, *Surface and Interface Analysis*, 1979, **1**, 2
- ⁷³ C. J. Powell, *J. Electr. Spectrosc.*, 1988, **47**, 197
- ⁷⁴ J. C. Ashley, *J. Electr. Spectrosc.*, 1982, **28**, 177
- ⁷⁵ A. Laikhtman, A. Lafosse, Y. Le Coat, and R. Azria and A. Hoffman, *J. Chem. Phys.*, 2003, **119**, 1794
- ⁷⁶ J. Ma, M. N. R. Ashfold and Y. A. Mankelevich, *J. Appl. Phys.*, 2009, **105**, 043302